



A Long Time Ago in a Galaxy Far, Far Away: A Candidate $z \sim 12$ Galaxy in Early JWST CEERS Imaging

Steven L. Finkelstein¹ , Micaela B. Bagley¹ , Pablo Arrabal Haro² , Mark Dickinson² , Henry C. Ferguson³ , Jeyhan S. Kartaltepe⁴ , Casey Papovich^{5,6} , Denis Burgarella⁷ , Dale D. Kocevski⁸ , Marc Huertas-Company^{9,10,11} , Kartheik G. Iyer¹² , Anton M. Koekemoer³ , Rebecca L. Larson^{1,13} , Pablo G. Pérez-González¹⁴ , Caitlin Rose⁴ , Sandro Tacchella^{15,16} , Stephen M. Wilkins^{17,18} , Katherine Chworowsky^{1,92} , Aubrey Medrano¹ , Alexa M. Morales¹ , Rachel S. Somerville¹⁹ , L. Y. Aaron Yung²⁰ , Adriano Fontana²¹ , Mauro Giavalisco²² , Andrea Grazian²³ , Norman A. Grogin³ , Lisa J. Kewley²⁴ , Allison Kirkpatrick²⁵ , Peter Kurczynski²⁶ , Jennifer M. Lotz²⁷ , Laura Pentericci²¹ , Nor Pirzkal²⁸ , Swara Ravindranath³ , Russell E. Ryan, Jr.³ , Jonathan R. Trump²⁹ , Guang Yang^{30,31}

and The CEERS Team:

Omar Almaini³² , Ricardo O. Amorín^{33,34} , Marianna Annunziatella³⁵ , Bren E. Backhaus²⁹ , Guillermo Barro³⁶ , Peter Behroozi^{37,38} , Eric F. Bell³⁹ , Rachana Bhatawdekar⁴⁰ , Laura Bisigello^{23,41} , Volker Bromm¹ , Véronique Buat⁷ , Fernando Buitrago^{42,43} , Antonello Calabrò⁴⁴ , Caitlin M. Casey¹ , Marco Castellano²¹ , Óscar A. Chávez Ortiz¹ , Laure Ciesla⁷ , Nikko J. Cleri^{5,6} , Seth H. Cohen⁴⁵ , Justin W. Cole^{5,6} , Kevin C. Cooke⁴⁶ , M. C. Cooper⁴⁷ , Asantha R. Cooray⁴⁷ , Luca Costantin³⁵ , Isabella G. Cox⁴ , Darren Croton^{48,49} , Emanuele Daddi⁵⁰ , Romeel Dave^{51,52} , Alexander de la Vega⁵³ , Avishai Dekel⁵⁴ , David Elbaz⁵⁵ , Vicente Estrada-Carpenter⁵⁶ , Sandra M. Faber⁵⁷ , Vital Fernández³³ , Keely D. Finkelstein¹ , Jonathan Freundlich⁵⁸ , Seiji Fujimoto^{59,60} , Ángela García-Argumániz^{61,62} , Jonathan P. Gardner²⁰ , Eric Gawiser⁶³ , Carlos Gómez-Guijarro⁶⁴ , Yuchen Guo¹ , Kurt Hamblin²⁵ , Timothy S. Hamilton⁶⁵ , Nimish P. Hathi³ , Benne W. Holwerda⁶⁶ , Michaela Hirschmann⁶⁷ , Taylor A. Hutchison^{5,6,13} , Anne E. Jaskot⁶⁸ , Saurabh W. Jha⁶³ , Shardha Jogee¹ , Stéphanie Juneau⁶⁹ , Intae Jung^{20,70,71} , Susan A. Kassin^{72,73} , Aurélien Le Bail⁵⁵ , Gene C. K. Leung¹ , Ray A. Lucas³ , Benjamin Magnelli⁵⁰ , Kameswara Bharadwaj Mantha⁷⁴ , Jasleen Matharu^{5,6} , Elizabeth J. McGrath⁸ , Daniel H. McIntosh⁷⁵ , Emiliano Merlin⁷⁶ , Bahram Mobasher⁷⁷ , Jeffrey A. Newman⁷⁸ , David C. Nicholls⁷⁹ , Viraj Pandya^{80,93} , Marc Rafelski^{3,81} , Kaila Ronayne^{5,6} , Paola Santini²¹ , Lise-Marie Seille⁷ , Ekta A. Shah⁸² , Lu Shen^{83,84} , Raymond C. Simons³ , Gregory F. Snyder³ , Elizabeth R. Stanway⁸⁵ , Amber N. Straughn²⁰ , Harry I. Teplitz⁸⁶ , Brittany N. Vanderhoof⁴ , Jesús Vega-Ferrero⁹ , Weichen Wang⁸⁷ , Benjamin J. Weiner⁸⁸ , Christopher N. A. Willmer⁸⁹ , Stijn Wuyts⁹⁰ , and Jorge A. Zavala⁹¹

¹ Department of Astronomy, The University of Texas at Austin, Austin, TX, USA; stevenf@astro.as.utexas.edu

² NSF's National Optical-Infrared Astronomy Research Laboratory, 950 North Cherry Avenue, Tucson, AZ 85719, USA

³ Space Telescope Science Institute, 3700 San Martin Drive, Baltimore, MD 21218, USA

⁴ Laboratory for Multiwavelength Astrophysics, School of Physics and Astronomy, Rochester Institute of Technology, 84 Lomb Memorial Drive, Rochester, NY 14623, USA

⁵ Department of Physics and Astronomy, Texas A&M University, College Station, TX 77843-4242, USA

⁶ George P. and Cynthia Woods Mitchell Institute for Fundamental Physics and Astronomy, Texas A&M University, College Station, TX 77843-4242, USA

⁷ Aix Marseille Univ, CNRS, CNES, LAM Marseille, France

⁸ Department of Physics and Astronomy, Colby College, Waterville, ME 04901, USA

⁹ Instituto de Astrofísica de Canarias, La Laguna, Tenerife, Spain

¹⁰ Universidad de la Laguna, La Laguna, Tenerife, Spain

¹¹ Université Paris-Cité, LERMA—Observatoire de Paris, PSL, Paris, France

¹² Dunlap Institute for Astronomy & Astrophysics, University of Toronto, Toronto, ON M5S 3H4, Canada

¹³ NSF Graduate Fellow

¹⁴ Centro de Astrobiología (CAB/CSIC-INTA), Ctra. de Ajalvir km 4, Torrejón de Ardoz, E-28850, Madrid, Spain

¹⁵ Kavli Institute for Cosmology, University of Cambridge, Madingley Road, Cambridge, CB3 0HA, UK

¹⁶ Cavendish Laboratory, University of Cambridge, 19 JJ Thomson Avenue, Cambridge, CB3 0HE, UK

¹⁷ Astronomy Centre, University of Sussex, Falmer, Brighton BN1 9QH, UK

¹⁸ Institute of Space Sciences and Astronomy, University of Malta, Msida MSD 2080, Malta

¹⁹ Center for Computational Astrophysics, Flatiron Institute, 162 5th Avenue, New York, NY 10010, USA

²⁰ Astrophysics Science Division, NASA Goddard Space Flight Center, 8800 Greenbelt Road, Greenbelt, MD 20771, USA

²¹ INAF-Osservatorio Astronomico di Roma, via di Frascati 33, I-00078 Monte Porzio Catone, Italy

²² University of Massachusetts Amherst, 710 North Pleasant Street, Amherst, MA 01003-9305, USA

²³ INAF-Osservatorio Astronomico di Padova, Vicolo dell'Osservatorio 5, I-35122, Padova, Italy

²⁴ Harvard-Smithsonian Center for Astrophysics, 60 Garden Street, Cambridge, MA 02138, USA

²⁵ Department of Physics and Astronomy, University of Kansas, Lawrence, KS 66045, USA

²⁶ Observational Cosmology Laboratory, Code 665, NASA Goddard Space Flight Center, Greenbelt, MD 20771, USA

²⁷ Gemini Observatory/NSF's National Optical-Infrared Astronomy Research Laboratory, 950 North Cherry Avenue, Tucson, AZ 85719, USA

²⁸ ESA/AURA Space Telescope Science Institute, USA

²⁹ Department of Physics, 196 Auditorium Road, Unit 3046, University of Connecticut, Storrs, CT 06269, USA

³⁰ Kapteyn Astronomical Institute, University of Groningen, P.O. Box 800, 9700 AV Groningen, The Netherlands

³¹ SRON Netherlands Institute for Space Research, Postbus 800, 9700 AV Groningen, The Netherlands

³² School of Physics and Astronomy, University of Nottingham, University Park, Nottingham NG7 2RD, UK

³³ Instituto de Investigación Multidisciplinar en Ciencia y Tecnología, Universidad de La Serena, Raul Bitrán 1305, La Serena 2204000, Chile

³⁴ Departamento de Astronomía, Universidad de La Serena, Av. Juan Cisternas 1200 Norte, La Serena 1720236, Chile

³⁵ Centro de Astrobiología (CSIC-INTA), Ctra de Ajalvir km 4, Torrejón de Ardoz, E-28850, Madrid, Spain

- ³⁶ Department of Physics, University of the Pacific, Stockton, CA 90340, USA
- ³⁷ Department of Astronomy and Steward Observatory, University of Arizona, Tucson, AZ 85721, USA
- ³⁸ Division of Science, National Astronomical Observatory of Japan, 2-21-1 Osawa, Mitaka, Tokyo 181-8588, Japan
- ³⁹ Department of Astronomy, University of Michigan, 1085 South University Avenue, Ann Arbor, MI 48109-1107, USA
- ⁴⁰ European Space Agency, ESA/ESTEC, Keplerlaan 1, 2201 AZ Noordwijk, The Netherlands
- ⁴¹ Dipartimento di Fisica e Astronomia “G. Galilei,” Università di Padova, Via Marzolo 8, I-35131 Padova, Italy
- ⁴² Departamento de Física Teórica, Atómica y Óptica, Universidad de Valladolid, E-47011 Valladolid, Spain
- ⁴³ Instituto de Astrofísica e Ciências do Espaço, Universidade de Lisboa, OAL, Tapada da Ajuda, PT1349-018 Lisbon, Portugal
- ⁴⁴ Osservatorio Astronomico di Roma, via Frascati 33, Monte Porzio Catone, Italy
- ⁴⁵ School of Earth and Space Exploration, Arizona State University, Tempe, AZ 85287, USA
- ⁴⁶ AAAS S&T Policy Fellow hosted at the National Science Foundation, 1200 New York Avenue NW, Washington, DC 20005, USA
- ⁴⁷ Department of Physics & Astronomy, University of California, Irvine, 4129 Reines Hall, Irvine, CA 92697, USA
- ⁴⁸ Centre for Astrophysics & Supercomputing, Swinburne University of Technology, Hawthorn, VIC 3122, Australia
- ⁴⁹ ARC Centre of Excellence for All Sky Astrophysics in 3 Dimensions (ASTRO 3D), Australia
- ⁵⁰ Université Paris-Saclay, Université Paris Cité, CEA, CNRS, AIM, F-91191, Gif-sur-Yvette, France
- ⁵¹ Institute for Astronomy, University of Edinburgh, Blackford Hill, Edinburgh, EH9 3HJ UK
- ⁵² Department of Physics and Astronomy, University of the Western Cape, Robert Sobukwe Road, Bellville, Cape Town 7535, South Africa
- ⁵³ Department of Physics and Astronomy, Johns Hopkins University, Baltimore, MD, USA
- ⁵⁴ Racah Institute of Physics, The Hebrew University of Jerusalem, Jerusalem 91904, Israel
- ⁵⁵ Université Paris-Saclay, Université Paris Cité, CEA, CNRS, AIM, F-91191, Gif-sur-Yvette, France
- ⁵⁶ Department of Astronomy & Physics, Saint Mary’s University, 923 Robie Street, Halifax, NS, B3H 3C3, Canada
- ⁵⁷ University of California Observatories and Department of Astronomy and Astrophysics, University of California, Santa Cruz, 1156 High Street, Santa Cruz, CA 95064, USA
- ⁵⁸ Université de Strasbourg, CNRS, Observatoire Astronomique de Strasbourg, UMR 7550, F-67000 Strasbourg, France
- ⁵⁹ Cosmic Dawn Center (DAWN), Jagtvej 128, DK-2200 Copenhagen N, Denmark
- ⁶⁰ Niels Bohr Institute, University of Copenhagen, Lyngbyvej 2, DK-2100 Copenhagen Ø, Denmark
- ⁶¹ Departamento de Física de la Tierra y Astrofísica, Facultad de CC Físicas, Universidad Complutense de Madrid, E-28040, Madrid, Spain
- ⁶² Instituto de Física de Partículas y del Cosmos IPARCOS, Facultad de CC Físicas, Universidad Complutense de Madrid, E-28040 Madrid, Spain
- ⁶³ Department of Physics and Astronomy, Rutgers, the State University of New Jersey, Piscataway, NJ 08854, USA
- ⁶⁴ Université Paris-Saclay, Université Paris Cité, CEA, CNRS, AIM, F-91191, Gif-sur-Yvette, France
- ⁶⁵ Shawnee State University, Portsmouth, OH, USA
- ⁶⁶ Physics & Astronomy Department, University of Louisville, Louisville, KY 40292, USA
- ⁶⁷ Institute of Physics, Laboratory of Galaxy Evolution, Ecole Polytechnique Fédérale de Lausanne (EPFL), Observatoire de Sauvigny, 1290 Versoix, Switzerland
- ⁶⁸ Department of Astronomy, Williams College, Williamstown, MA 01267, USA
- ⁶⁹ NSF’s NOIRLab, 950 North Cherry Avenue, Tucson, AZ 85719, USA
- ⁷⁰ Department of Physics, The Catholic University of America, Washington, DC 20064, USA
- ⁷¹ Center for Research and Exploration in Space Science and Technology, NASA/GSFC, Greenbelt, MD 20771, USA
- ⁷² Space Telescope Science Institute, Baltimore, MD 21218, USA
- ⁷³ Department of Physics & Astronomy, Johns Hopkins University, 3400 North Charles Street, Baltimore, MD 21218, USA
- ⁷⁴ Minnesota Institute for Astrophysics, University of Minnesota, 116 Church Street SE, Minneapolis, MN 55455, USA
- ⁷⁵ Division of Energy, Matter and Systems, School of Science and Engineering, University of Missouri–Kansas City, Kansas City, MO 64110, USA
- ⁷⁶ INAF Osservatorio Astronomico di Roma, Via Frascati 33, I-00078 Monteporzio Catone, Rome, Italy
- ⁷⁷ Department of Physics and Astronomy, University of California, 900 University Avenue, Riverside, CA 92521, USA
- ⁷⁸ Department of Physics and Astronomy and PITT PACC, University of Pittsburgh, Pittsburgh, PA 15260, USA
- ⁷⁹ Research School of Astronomy and Astrophysics, Australian National University, Canberra, ACT 2600, Australia
- ⁸⁰ Columbia Astrophysics Laboratory, Columbia University, 550 West 120th Street, New York, NY 10027, USA
- ⁸¹ Department of Physics and Astronomy, Johns Hopkins University, Baltimore, MD 21218, USA
- ⁸² Department of Physics and Astronomy, University of California, Davis, One Shields Avenue, Davis, CA 95616, USA
- ⁸³ CAS Key Laboratory for Research in Galaxies and Cosmology, Department of Astronomy, University of Science and Technology of China, Hefei 230026, People’s Republic of China
- ⁸⁴ School of Astronomy and Space Sciences, University of Science and Technology of China, Hefei, 230026, People’s Republic of China
- ⁸⁵ Department of Physics, University of Warwick, Coventry, CV4 7AL, UK
- ⁸⁶ IPAC, Mail Code 314-6, California Institute of Technology, 1200 East California Boulevard, Pasadena, CA 91125, USA
- ⁸⁷ Department of Physics and Astronomy, Johns Hopkins University, 3400 North Charles Street, Baltimore, MD 21218, USA
- ⁸⁸ MMT/Steward Observatory, University of Arizona, 933 North Cherry Avenue, Tucson, AZ 85721, USA
- ⁸⁹ Steward Observatory, University of Arizona, 933 North Cherry Avenue, Tucson, AZ 85721, USA
- ⁹⁰ Department of Physics, University of Bath, Claverton Down, Bath BA2 7AY, UK
- ⁹¹ National Astronomical Observatory of Japan, 2-21-1 Osawa, Mitaka, Tokyo 181-8588, Japan

Received 2022 July 25; revised 2022 August 23; accepted 2022 September 2; published 2022 December 1

Abstract

We report the discovery of a candidate galaxy with a photo- z of $z \sim 12$ in the first epoch of the James Webb Space Telescope (JWST) Cosmic Evolution Early Release Science Survey. Following conservative selection criteria, we identify a source with a robust $z_{\text{phot}} = 11.8^{+0.3}_{-0.2}$ (1σ uncertainty) with $m_{\text{F200W}} = 27.3$ and $\gtrsim 7\sigma$ detections in five filters. The source is not detected at $\lambda < 1.4 \mu\text{m}$ in deep imaging from both Hubble Space Telescope (HST) and

⁹² NSF Graduate Fellow.

⁹³ Hubble Fellow.



JWST and has faint $\sim 3\sigma$ detections in JWST F150W and HST F160W, which signal a Ly α break near the red edge of both filters, implying $z \sim 12$. This object (Maisie’s Galaxy) exhibits $F115W - F200W > 1.9$ mag (2σ lower limit) with a blue continuum slope, resulting in 99.6% of the photo- z probability distribution function favoring $z > 11$. All data-quality images show no artifacts at the candidate’s position, and independent analyses consistently find a strong preference for $z > 11$. Its colors are inconsistent with Galactic stars, and it is resolved ($r_h = 340 \pm 14$ pc). Maisie’s Galaxy has $\log M_*/M_\odot \sim 8.5$ and is highly star-forming ($\log \text{sSFR} \sim -8.2 \text{ yr}^{-1}$), with a blue rest-UV color ($\beta \sim -2.5$) indicating little dust, though not extremely low metallicity. While the presence of this source is in tension with most predictions, it agrees with empirical extrapolations assuming UV luminosity functions that smoothly decline with increasing redshift. Should follow-up spectroscopy validate this redshift, our universe was already aglow with galaxies less than 400 Myr after the Big Bang.

Unified Astronomy Thesaurus concepts: [Early universe \(435\)](#); [Galaxy formation \(595\)](#); [Galaxy evolution \(594\)](#)

1. Introduction

The study of galaxy evolution is the ultimate human origin story—not just how did our species, planet, or solar system come to be, but this field seeks to answer how our Milky Way came to be. One method to study our Galactic origins is to study the earliest building blocks of the Milky Way by searching for and analyzing galaxies forming in the early universe. The advent of the Wide Field Camera 3 (WFC3) on the Hubble Space Telescope (HST) pushed our cosmic horizons well into the epoch of reionization, the time when energetic photons (presumably from massive stars in early galaxies) ionized the gas in the intergalactic medium (e.g., Finkelstein 2016; Stark 2016; Robertson 2022, and references therein). These studies found that the $z = 6\text{--}10$ universe is teeming with galaxies, with thousands of galaxy candidates known, including spectroscopic confirmations out to $z \sim 11$ (Oesch et al. 2016; Jiang et al. 2021).

One key focus in these studies has been the evolution of the cosmic star formation rate density (SFRD). This quantity is well known to rise from the present day to the peak of cosmic star formation at $z \sim 2\text{--}3$, then decline again to early times (e.g., Madau & Dickinson 2014). As the aforementioned WFC3 studies pushed to higher redshifts, it became of interest to study whether the cosmic SFRD, which exhibited a smooth decline from $z = 4\text{--}8$ (e.g., Bouwens et al. 2015; Finkelstein et al. 2015), continued to decline smoothly to even higher redshifts. Results in the literature were mixed, with some studies finding evidence for an accelerated decline in the SFRD (e.g., Oesch et al. 2018; Bouwens et al. 2021), while others found that observations supported a continued smooth decline (e.g., Coe et al. 2013; McLeod et al. 2016; Finkelstein & Bagley 2022). Simulations do make predictions for the evolution of the SFRD, but these predictions span a wide range (e.g., Gnedin 2016; Dayal & Ferrara 2018; Tacchella et al. 2018; Yung et al. 2019; Behroozi et al. 2020).

Part of the difficulty of such studies is the near-heroic observational effort needed to study galaxies at $z \sim 10$ with HST. These galaxies become more and more difficult to see with this 2.4 m ultraviolet (UV)/optical/near-IR telescope, and at these high redshifts, they become single-band detections, leaving the $z \gtrsim 11$ universe opaque to our understanding. To avoid being dominated by spurious sources, studies employ a variety of vetting criteria to ensure robust samples of candidate galaxies (e.g., Bouwens et al. 2021; Bagley et al. 2022; Finkelstein et al. 2022), which makes it difficult to estimate the sample completeness and thereby to obtain a robust estimate of the SFRD.

This all changes with the advent of the James Webb Space Telescope (JWST). The dramatic increase in light-gathering

power coupled with the infrared sensitivity makes this telescope the ideal machine to push our cosmic horizons to the epoch of the first galaxies. As the first JWST images arrive, it is natural to wonder what these early data tell us about the rise of star formation in the early universe. If the SFRD really declines as steeply at $z > 8$ as has been proposed, few galaxies at $z > 11$ should be detectable in early JWST data. If the decline is instead more gradual, one might expect to discover galaxies at $z \sim 12$ or even higher. In just the first week since the data have been released, exciting results already indicate significant star formation is occurring at $z > 11$ (e.g., Castellano et al. 2022; Naidu et al. 2022).

As another early probe of this epoch, here we report on a search for the highest-redshift ($z \gtrsim 12$) galaxies in the first epoch of imaging from the Cosmic Evolution Early Release Science Survey (CEERS; S. Finkelstein et al. 2022, in preparation). These data were among the first Cycle 1 science exposures taken and included in the first publicly released data on July 14. Section 2 describes the observations and data reduction, while Section 3 describes our photometry, photometric redshift measurement, and sample selection procedure. Section 4 presents our results, and we discuss these results in Section 5. Our conclusions are presented in Section 6. In this paper, we assume the latest Planck flat Λ CDM cosmology with $H_0 = 67.36$, $\Omega_m = 0.3153$, and $\Omega_\Lambda = 0.6847$ (Planck Collaboration et al. 2020). All magnitudes are in the absolute bolometric system (AB; Oke & Gunn 1983).

2. Observations

2.1. CEERS Data

CEERS is one of 13 early release science surveys designed to obtain data covering all areas of astronomy early in Cycle 1. CEERS is based around a mosaic of 10 NIRCcam (Rieke et al. 2005) pointings, with six obtaining NIRSspec (Jakobsen et al. 2022) in parallel and four with MIRI (Rieke et al. 2015) in parallel (four of these pointings also include NIRCcam wide-field slitless grism spectroscopy; Greene et al. 2016). Here we make use of the first four CEERS NIRCcam pointings, obtained on 2022 June 21, known as CEERS1, CEERS2, CEERS3, and CEERS6.

In each pointing, data were obtained in the short-wavelength (SW) channel F115W, F150W, and F200W filters and long-wavelength (LW) channel F277W, F356W, F410M, and F444W filters. The total exposure time for pixels observed in all three dithers was typically $2835 \text{ s filter}^{-1}$. The exception is F115W, which obtained double the exposure time to increase the depth on the filter covering the wavelength range below the Ly α break at $z > 10$. The full details of the readout and dither

patterns will be available in the CEERS overview paper (S. Finkelstein et al. 2022, in preparation).

2.2. Data Reduction

We performed a careful initial reduction of the NIRC*am* images in all four pointings using version 1.6.2 of the JWST Calibration Pipeline⁹⁴ with some custom modifications. We used the current (2022 July 29) set of NIRC*am* reference files,⁹⁵ which includes in-flight read noise, superbias, distortion, and photometric flux calibration references. We note that the flats were created preflight. We describe our reduction steps below and present more details in M. Bagley et al. (2022, in preparation).

Beginning with the raw data, we used Stage 1 of the pipeline with all default parameters to apply detector-level corrections, fit the ramps in each integration, and output count-rate maps. We next subtracted the “wisp” features, stray light that is reflected off the secondary mirror supports, from detectors A3, B3, and B4 for filters F150W and F200W. For each image I , we scaled the corresponding wisp template⁹⁶ W (available as of 2022 July 8) by the coefficient a that minimized $\text{Var}(I - aW)$ and subtracted the scaled template. We then performed a custom step to remove $1/f$ noise, which is correlated noise introduced in the images during the detector readout that presents as horizontal and vertical striping patterns (Schlawin et al. 2020). We applied the flat field to the count-rate maps to ensure we were measuring the $1/f$ noise pattern on a flat image. We masked all bad pixels and source flux using PHOTUTILS (Bradley et al. 2020) to detect sources and implementing a tiered approach to source masking. This approach convolves the image with progressively smaller kernels, identifying sources at each step. We use four tiers with Gaussian kernels of $\sigma = 25, 15, 5,$ and 2 pixels (on the original $0''.031$ and $0''.063 \text{ pixel}^{-1}$ scales for the SW and LW channels, respectively). These values were chosen after experimenting with several filter kernels to aggressively mask as much source flux as possible. First, for each row and then each column, we measured a σ -clipped median value and subtracted this value from the un-flat-fielded count-rate map. This correction was performed amplifier by amplifier in all filters except F444W, for which we did not perform any correction because the significant residual flat-field structure present in the images dominated any $1/f$ pattern.

After processing the cleaned count-rate maps through Stage 2 of the pipeline, we performed an astrometric calibration using an edited version of the TweakReg step of the pipeline. The TweakReg step detects sources in each input image, identifies their counterparts in the reference catalog, and calculates a transformation to correct the image WCS. We ran SEXTRACTOR (SE; Bertin & Arnouts 1996) on each individual image to replace the internal TweakReg source identification, finding that SE did a better job of identifying and deblending real sources. In lieu of using the default options that allow for alignment to Gaia DR2, we used a reference catalog derived from an HST F160W $0''.03 \text{ pixel}^{-1}$ mosaic⁹⁷ in the EGS field with astrometry tied to Gaia-EDR3 (see Koekemoer et al. 2011,

for details). We first determined the relative offsets between images of the same detector, allowing for shifts in x and y . The rms of this relative astrometry is $\sim 3\text{--}6$ mas. We then aligned all images to our HST F160W reference catalog, allowing for shifts in x and y , rotations, and, in the LW images only, a scaling to account for any additional distortion (though we note that the scaling factor is $\sim 1 \times 10^{-5}$). The rms of this absolute alignment is $\sim 12\text{--}15$ mas, and the alignment between NIRC*am* images in different filters has an rms of $5\text{--}10$ mas.

We fit and removed a single value in MJy sr^{-1} from each calibrated detector image separately before coadding the images onto a common output grid. For each image, we additionally calculate a scaling factor for the read-noise variance array (`VAR_RNOISE`) from the background-subtracted sky pixels, again avoiding source flux and bad pixels. We apply this scaling factor to the variance arrays so that they include the robustly measured sky variance. The coadding was performed using the drizzle algorithm with an inverse variance map weighting (Casertano et al. 2000; Fruchter & Hook 2002) via the Resample step in the pipeline. The output mosaics have pixel scales of $0''.03 \text{ pixel}^{-1}$. The usable total area covered by these observations, calculated from the number of pixels with low effective error map values in F115W, F150W, F200W, F277W, and the detection image (see below), is 34.5 arcmin^2 .

We note that our data reduction represents a preliminary version, with several aspects that will be improved with the release of updated NIRC*am* reference files. We also have not removed the features known as “snowballs” from the mosaics at this time. However, we have carefully inspected all input exposures to ensure that the fluxes in all filters at the positions of galaxies of interest are unaffected by snowballs (see Section 4.2).

3. Methodology

3.1. Photometric Catalog Construction

The full details of our photometric analysis will be presented in S. Finkelstein et al. (2022d, in preparation); here we briefly summarize our procedures (many of which are similar to Finkelstein et al. 2022). The data products from our modified data reduction pipeline come in the form of multi-extension “i2d” files. We first estimate and subtract any residual background using a custom Python-based algorithm. This routine iteratively convolves the image with Gaussian kernels of progressively smaller sizes (with $\sigma = 25, 15, 5,$ and 2 pixels), then uses PHOTUTILS to mask pixels identified with sources in four iterations to mask progressively smaller sources, dilating the masks in between iterations (by 33, 25, 21, and 19 pixels), then measuring the background after masking with PHOTUTILS.BACKGROUND2D. This final background image-construction step used the BkgZoomInterpolator algorithm to construct a smooth background based on the robust σ -clipped means measured within boxes of 10×10 pixels and median-filtered over 5×5 adjacent boxes.

The i2d file was split into separate extensions, subtracting this background from the SCI extension. Empirical point-spread functions (PSFs) were made by stacking stars, and the F115W, F150W, F200W, and F277W images were PSF-matched to the F356W image using PYPHER. Photometry was computed on the PSF-matched images using SE (Bertin & Arnouts 1996) v2.25.0 in two-image mode, with an inverse variance-weighted combination of the PSF-matched F277W

⁹⁴ jwst-pipeline.readthedocs.io

⁹⁵ jwst-crds.stsci.edu, jwst_nircam_0221.imap.

⁹⁶ jwst-docs.stsci.edu/jwst-near-infrared-camera/nircam-features-and-caveats/nircam-claws-and-wisps

⁹⁷ ceers.github.io/hdr1.html

and F356W images as the detection image, with photometry measured on all seven bands.

Colors were measured in small Kron apertures with a Kron factor of 0.8 and a Kron minimum radius of 1.1 pixels; this is smaller than previous studies, which we found necessary to keep the elliptical aperture close to the significant isophotes of small, faint galaxies. An aperture correction was derived in the F356W catalog as the ratio between the flux measured in the default Kron aperture (with PHOT_AUTOPARAMS 2.5, 3.5) and that in our small Kron aperture. This correction was applied to all fluxes and uncertainties. We use the CEERS simulated imaging⁹⁸ to test the accuracy of this procedure, finding that after this aperture correction, the total fluxes were underestimated by $\sim 10\%$ – 15% , rising to 22% in F444W (understandable due to the larger PSF in F444W as the photometric apertures were defined on F356W). We apply these simulation-based corrections (comparable to similar corrections applied in HST studies; e.g., Finkelstein et al. 2022) to all fluxes and uncertainties to complete our total flux measurements. All fluxes and uncertainties were corrected for Galactic attenuation assuming a field-averaged $E(B - V) = 0.006$ and a Cardelli et al. (1989) Milky Way attenuation curve. We also measure fluxes in a range of circular apertures; as these are used for detection significance tests, we do not correct them to total fluxes (though they are still corrected for Galactic attenuation).

We derive flux uncertainties directly from the data, following Finkelstein et al. (2022), based on previous methodology outlined in Papovich et al. (2016). We fit for the noise as a function of aperture size by measuring the fluxes at $\sim 5 \times 10^3$ randomly placed positions in 15 circular apertures with diameters ranging from 1 to 100 pixels, fitting a polynomial function to the standard deviation in aperture fluxes as a function of the number of pixels in each aperture. We then use this function to calculate the photometric uncertainties for each object for a given aperture area. These values were scaled by the ratio of the error image value at the central position of a given source to the median error value of the whole map. All aperture and Galactic attenuation corrections were applied to these uncertainties. Finally, around each source in our catalog, we calculate a “local” noise estimate as the standard deviation in flux values from the 200 closest of these previously placed random apertures.

3.2. Photometric Redshifts

We use the EAZY (Brammer et al. 2008) software package to estimate photometric redshifts for all sources in our photometric catalog. EAZY fits nonnegative linear combinations of user-supplied templates to derive probability distribution functions (PDFs) for the redshift based on the quality of fit of the various template combinations to the observed photometry for a given source. The template set we use includes the “tweak_fsps_QSF_12_v3” set of 12 FSPP (Conroy & Gunn 2010) templates recommended by the EAZY documentation. To this, we add a set of six additional templates spanning bluer colors than the FSPP models, as R. Larson et al. (2022, in preparation) found that these improve the accuracy of photometric redshift fits for the expected blue colors of $z > 9$ galaxies.

The new templates were created using stellar population models created with BPASS (Eldridge & Stanway 2009). To generate bluer rest-UV colors than the initial set of FSPP templates, we selected BPASS templates that had low metallicities (5% solar) and young stellar populations (log stellar ages of 6, 6.5, and 7 Myr) and were inclusive of binary stars. We added an additional set of these models inclusive of nebular emission lines derived with CLOUDY (Ferland et al. 1998) using a high ionization parameter ($\log U = -2$), a similarly low metallicity, and nebular continuum emission. R. Larson et al. (2022, in preparation) validated the efficacy of including these models by testing the recovery of photometric redshifts from a mock catalog derived by a semianalytic model (Yung et al. 2022), finding that the inclusion of these six additional templates significantly improved the photometric redshift estimates for blue high-redshift galaxies.

We do not use a luminosity prior (e.g., a flat prior is assumed), as the epoch in question is completely unexplored, and we include a systematic error of 5% of the observed flux values. Our fiducial EAZY run uses our total fluxes derived from our Kron aperture-measured colors, and we use the measured fluxes and errors even in the case of nondetections (as opposed to using upper limits). We also perform two ancillary runs, which we use for later vetting. One uses fluxes measured in $0''.3$ circular apertures (to cover the possibility that a Kron ellipse was drawn inaccurately, which happens in the presence of bright neighbors). A second run had a maximum redshift of $z = 7$ to allow the exploration of secondary redshift solutions.

3.3. Sample Selection

To select our sample of candidate very high redshift galaxies, we follow previous work done by our team (Finkelstein et al. 2015, 2022; Rojas-Ruiz et al. 2020; Bagley et al. 2022). We make use of photometric signal-to-noise (S/N) criteria to ensure robust photometric detections (to minimize the chance of a spurious signal) and nondetections below the Ly α break. We add to these several criteria based off of the full EAZY redshift PDF (denoted $\mathcal{P}(z)$). We note that the criteria imposed here are fairly conservative; we wish to identify the most robust highest-redshift candidates. Future work will explore how to relax some of these criteria to improve sample completeness and push to $z < 12$ without introducing unacceptable levels of contamination.

To derive an initial sample of $z \geq 12$ galaxies, we first impose all of following requirements.

1. An S/N in both F200W and F277W of > 6 in conservatively small $0''.2$ (6.7 pixel) diameter apertures for these measurements using both the fiducial (global) and local noise estimates. We note that enforcing an S/N cut in F200W effectively limits this sample to $z \lesssim 15$, though by enforcing detections in both an SW and an LW detector, we limit the inclusion of detector-specific spurious sources.
2. Error map values of < 1000 (indicating coverage by the majority of exposures) in F115W, F150W, F200W, F277W, and the detection image.
3. Initial more inclusive photometric redshift cuts of $\int \mathcal{P}(z > 8) \geq 0.9$, $z_{\text{best}} > 8.5$, and $\chi_{\text{eazy}}^2 < 20$ (to reject poor EAZY fits), and that the integrated $\mathcal{P}(z)$ in a $\Delta z = 1$

⁹⁸ Simulated Data Release 3; ceers.github.io/sdr3.html.

width bin centered on integer redshift values (z_{sample}) with the largest integrated $\mathcal{P}(z)$ to be at $z_{\text{sample}} \geq 9$.

4. Objects at $z_{\text{sample}} > 10$ must have $S/N \leq 2.0$ in F115W, while objects at $z_{\text{sample}} > 13$ must have $S/N \leq 2.0$ in both F115W and F150W (in both the global and local noise in $0''.2$ diameter apertures). These redshifts correspond to the wavelength of the Ly α break leaving a given dropout filter.
5. An F200W magnitude of < 29 , to focus on well-detected objects regardless of formal S/N .

After this initial set of selection criteria, we examined the resulting objects. We inspected their spectral energy distributions (SEDs), image stamps, and $\mathcal{P}(z)$ plots. We noticed several low-confidence sources that could be identified with further automated cuts. We thus implemented the following additional set of selection criteria.

1. We additionally implement all of the above detection significance criteria, in both the detection and dropout bands, in a $0''.3$ diameter aperture to account for situations where faint flux was visible slightly off-center of the source barycenter.
2. We require the χ^2 from an additional EAZY run with a maximum redshift of 7 to have a significantly worse fit than our fiducial run via $\chi^2_{\text{Low-}z} - \chi^2_{\text{fiducial}} > 4$.
3. We impose a single color cut of $F200W - F444W < 1$ for objects with $z_{\text{sample}} \leq 13$ to reduce the incidence of red low-redshift interlopers. This is similar to the color cuts simulated by Hainline et al. (2020) and implemented by Castellano et al. (2022). For objects with $z_{\text{sample}} = 13-18$, the Ly α break falls in the F200W filter; thus, we require $F277W - F444W < 1$.
4. To account for situations where the Kron aperture could be affected by nearby bright sources, we also require $\int \mathcal{P}(z > 8) \geq 0.5$ from an independent EAZY run performed with colors measured in $0''.3$ circular apertures.

As our focus here is on the highest-redshift sources, we limit our analysis to objects with $z_{\text{sample}} \geq 12$. Running the above selection process on all four fields, we find a single galaxy candidate that satisfies all of the above criteria. We perform an initial visual inspection of this candidate, inspecting $1''.5$ image stamps in all filters and $5''$ image cutouts in F200W and the detection image, and find that this object appears astrophysical in origin and is not an artifact.

4. Results

4.1. A Robust Galaxy Candidate at $z \approx 12$

This source, CEERS J141946.36+525632.8, hereafter known as ‘‘Maisie’s Galaxy,’’⁹⁹ was detected in the CEERS2 field. Promisingly, it was first identified in the earliest (v0.02) internal CEERS reduction in this field, being the first $z \gtrsim 12$ candidate viewed on 2022 July 18. In each subsequent reduction, this source continued to satisfy all selection criteria, becoming progressively more robust as the data became cleaner. Several CEERS team members viewed this potential $z \gtrsim 12$ candidate on 2022 July 22 and agreed on the robustness

Table 1
Properties of Maisie’s Galaxy

Property	Value
Source ID	CEERS J141946.36+525632.8
R.A. (J2000 [deg])	214.943153
Decl. (J2000 [deg])	52.942442
z_{eazy}	$11.8^{+0.2}_{-0.3}$
$\mathcal{T}_{\text{Big Bang}}$	373^{+16}_{-8} Myr
M_{UV} (mag)	$-20.32^{+0.08}_{-0.06}$
β	$-2.47^{+0.09}_{-0.09}$
$\log(M^*/M_{\odot})$	$8.50^{+0.29}_{-0.44}$
A_v (mag)	$0.07^{+0.23}_{-0.06}$
$\text{SFR}_{10 \text{ Myr}}$ ($M_{\odot} \text{ yr}^{-1}$)	$2.1^{+4.8}_{-2.0}$
$\log \text{sSFR}_{10 \text{ Myr}}$ (yr^{-1})	$-8.2^{+1.0}_{-1.6}$
Mass-weighted age (Myr)	18^{+18}_{-9}

Note. Here $\mathcal{T}_{\text{Big Bang}}$ is the time elapsed from the Big Bang to the photometric redshift for our assumed cosmology, and M_{UV} and β were computed from the PROSPECTOR models using the same techniques as in Tacchella et al. (2022). The physical properties listed below the horizontal line were derived with PROSPECTOR.

of this source. The photometric redshift of this source with NIRCam photometry alone is $z = 12.0^{+0.2}_{-0.4}$.

Given the much greater sensitivity of NIRCam, we do not expect significant changes to our interpretation based on the inclusion of HST images. These images were not included in our fiducial SE analysis, as they had not yet been pixel-aligned given the short time since NIRCam data acquisition. However, upon inspection, we find a hint of a positive signal at the position of the source in the F160W image. Indeed, while the source is not in the published Stefanon et al. (2017) and Skelton et al. (2014) catalogs, there is a 3.5σ detection at a separation of $0''.15$ in the Finkelstein et al. (2022) catalog (this object has $S/N < 2$ in all other HST filters in this catalog).

Using SE, we perform forced photometry at this position on the CANDELS (e.g., Grogin et al. 2011; Koekemoer et al. 2011) 30 mas images (using the updated images provided by the CEERS team, which has registered the astrometry to Gaia) in the ACS F606W and F814W and WFC3 F125W, F140W, and F160W bands. Following Finkelstein et al. (2022), we apply an additional flux correction of 1.2 to all HST bands to account for the missing wings of the PSF in the larger Kron aperture. We find $S/N < 2$ in all bands except WFC3 F160W, which has an $\sim 4\sigma$ detection, with a flux consistent with the weak F150W detection for this source. Including this photometry (listed in Table 3) in our photometric redshift fit slightly changes our photometric redshift estimate to $z = 11.8^{+0.2}_{-0.3}$, which (for our assumed cosmology) corresponds to an age of the universe of 373^{+16}_{-8} Myr. We use these results inclusive of HST photometry as our fiducial values. The properties of this galaxy are summarized in Table 1, and we list its photometry in Tables 2 and 3.

Figure 1 shows cutouts of this candidate galaxy in the NIRCam bands, while Figure 2 shows two color composites. Figure 3 shows the observed SED of our candidate with photometric redshift fits. The confidence of this source as a robust very high redshift galaxy is easy to see from all three of these figures. The Ly α break color, here F115W – F200W, is > 1.9 mag (2σ lower limit), completely eliminating any known low-redshift interloper (the F150W – F200W color is 1.3 mag,

⁹⁹ This exceptional source survived all detailed analysis steps, firmly becoming a plausible candidate on the ninth birthday of the lead author’s daughter. We adopt this short name for convenience in this and future papers.

Table 2
Measured Photometry of Maisie’s Galaxy with JWST/NIRCam

F115W	F150W	F200W	F277W	F356W	F410M	F444W
-7.52 ± 3.80	13.77 ± 4.40	45.11 ± 3.69	31.62 ± 2.68	26.29 ± 2.70	27.26 ± 5.30	26.78 ± 3.61

Note. Fluxes are in nJy and correspond to total fluxes. The AB magnitudes can be derived via $-2.5 \log_{10}(f_b[\text{nJy}]) + 31.4$.

Table 3
Measured Photometry of Maisie’s Galaxy with HST

F606W	F814W	F125W	F140W	F160W
7.3 ± 5.9	4.8 ± 8.0	-7.8 ± 9.2	-37.2 ± 16.0	33.8 ± 8.2

Note. Fluxes are in nJy and correspond to total fluxes. The AB magnitudes can be derived via $-2.5 \log_{10}(f_b[\text{nJy}]) + 31.4$.

still strong, though smaller in amplitude due to the Ly α break being present at the very red edge of F150W). Such a model would need to have an extremely red color to match our F115W – F200W > 1.9 mag break but then have a very blue color. While lower-redshift passive or dusty galaxies can mimic high-redshift Ly α breaks, the observed >1.9 mag break is much larger than known populations of low-redshift galaxies. Such galaxies would also be fairly red redward of the break.

Though differential geometry could accommodate UV spectral slopes as blue as $\beta \sim -1$, this object has $\beta \sim -2.5$ (see Section 5 of Casey et al. 2014). The significant detection in four broadband filters also rules out low-redshift extreme emission line galaxies. We show as the orange curve in Figure 3 EAZY’s best-fitting low-redshift model, which is ruled out at high confidence. Based on the nondetection in F115W and strong detection in F200W, the implied redshift is $z > 11$. This is confirmed by the EAZY fit, shown as the blue line, which prefers $z \sim 11.8$.

4.2. Fidelity of Candidate

Figure 1 shows 1''8 cutout images of this source at multiple wavelengths. This source shows the expected pattern for a high-redshift galaxy, with no significant flux in multiple dropout bands and robust flux in redder bands. The very sharp break between F115W and F200W is consistent with a redshift of $z > 11$ (the faint detection in F150W pushes the redshift solution to $z \sim 12$, as opposed to higher redshift). The advantage of JWST is clear here, as this source is well detected in all five NIRCam filters redward of the break. This multiband detection essentially eliminates the possibility of a spurious nature. Of note is that while persistence from previous observations affected several HST programs (see discussion in Bagley et al. 2022 and Finkelstein et al. 2022), CEERS observed with the bluest filters first; thus, any flux from persistence would be most apparent in F115W.

To further rule out a spurious nature, the science, error, and data-quality images were visually inspected at the position(s) of the best candidate(s). This is to ensure that the detected sources in the coadded images are not just chance superpositions of regions that were affected by cosmic rays or other artifacts. In the case of the $z \sim 12$ candidate, the source is visible in all of the individual F200W, F277W, and F356W exposures and overlaps with a cosmic ray in only a few images. Even in those cases, the cosmic rays that are masked in the data-quality array are of the typical size that is cleanly rejected in the jump-

detection step of the pipeline. There were no overlaps with the larger “snowball” charged-particle events.

As an additional check, we measured photometry at the position of this source on our images without our postprocessing residual background subtraction step to ensure that any systematic effects at this source position did not affect our results. The images already have a pedestal background-subtracted in the pipeline, so the relative colors should be secure when measured in this way. We found that this set of photometry was consistent with our fiducial photometry, and EAZY returns $\int \mathcal{P}(z > 11) = 0.995$. Therefore, it is unlikely that our sky-subtraction routine negatively affected our result.

Dust-reddened foreground galaxies are another potential source of contamination. However, Maisie’s Galaxy is not significantly detected in the deepest mid- and far-infrared, submillimeter, and radio data available for this sky region, including Spitzer MIPS 24 μm (Magnelli et al. 2009); Herschel PACS 100 and 160 μm (Lutz et al. 2011); Herschel SPIRE 250, 350, and 500 μm (Oliver et al. 2012); JCMT SCUBA2 850 μm (Geach et al. 2017); and VLA 10 cm (M. Dickinson 2022, private communication). The SCUBA2 nondetection is explored in more detail in Zavala et al. (2022).

4.2.1. Stellar Screening

Low-mass stars and brown dwarfs can have colors that mimic high-redshift galaxies in broadband filters (e.g., Yan et al. 2003; Ryan et al. 2005; Caballero et al. 2008; Wilkins et al. 2014) in the absence of longer-wavelength observations ($\lambda_{\text{obs}} \gtrsim 2 \mu\text{m}$). We explore this possibility following the methodology in Finkelstein et al. (2022). In brief, we derive a grid of models for the colors of low-mass stars and brown dwarfs (spectral types of M4–T8) in the NIRCam filters by integrating the IRTF SpEX brown dwarf templates (Burgasser 2014). As these spectra end at 2.5 μm , we use the tabulated 2MASS photometry to link each SpeX model with Spitzer/IRAC photometry from Patten et al. (2006). As the differences in filter transmission are negligible, we assume that we can map IRAC 3.6 μm onto F356W and 4.5 μm onto F444W; however, this assumption will need to be revisited with future spectroscopic observations of brown dwarfs with JWST at $\lambda \gtrsim 2.5 \mu\text{m}$. We estimate that the best brown dwarf template would be an L7.5 dwarf, and such a source would have blue near-infrared color of F115W – F200W = 0.9 mag. This is strongly ruled out by our observation of F115W – F200W > 1.9 mag (2σ lower limit). Additionally, our size analysis in Section 5.2 shows that this object is inconsistent with a point source.

4.2.2. Photometric Accuracy

While our fiducial photometric measurements were derived in as robust a manner as possible, different software packages require different parameters and assumptions, which could lead to unknown systematic biases. We thus independently derive NIRCam photometry from our images with two independent software packages. The first method is PHOTUTILS from

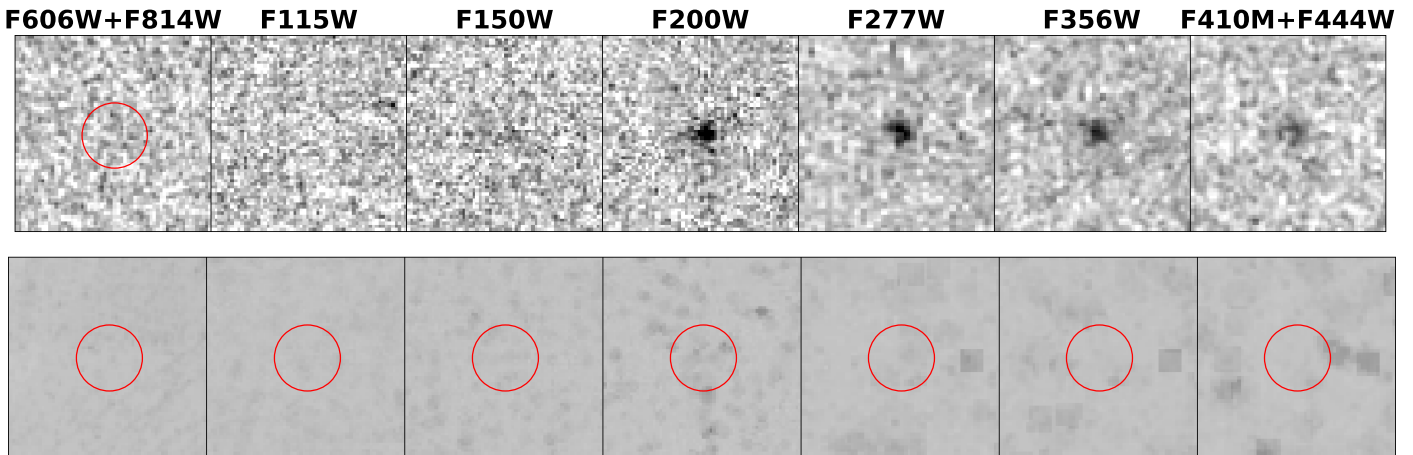


Figure 1. (Top) $1''.8 \times 1''.8$ cutout images centered on the position of Maisie’s Galaxy in the non-PSF-matched images. This source exhibits the hallmark colors of a distant galaxy: no discernible flux in a dropout band (we show stacked F606W+F814W, as well as F115W images; the circle has a radius of $0''.3$) and a significant detection in the bluest detection band (F200W in this case). Very faint flux is visible (at $\sim 2.8\sigma$ significance when measured in a $0''.2$ diameter aperture) in F150W, which drives the redshift to $z \sim 12$. The wide wavelength range of NIRCcam allows this source to be well detected in multiple filters, and in the imaging alone, it is clear that this source exhibits a blue spectral shape. (Bottom) Same ordering as the top panel for sky-uncertainty maps constructed from the variance of the readout noise, all using a linear scale from 0.33 to $3\times$ the robustly measured sky standard deviation in each band. The patchiness of the uncertainties is due to a loss of exposure time when cosmic rays are detected and rejected in the multiple readouts or in outlier rejection when combining the dithered exposures (the $2\times$ larger original pixel scale of the LW channels results in larger patches than the SW channels). The uncertainty arrays show no excess in rejected pixels near the candidate galaxy.

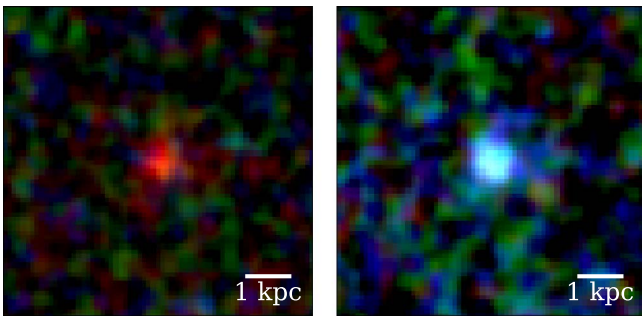


Figure 2. Three-color images of Maisie’s Galaxy. The left image is a composite of HST/ACS F606W and F814W in blue, F115W and F150W in green, and F200W in red. This shows the galaxy candidate as red due to the very high redshift resulting in no detected flux in the filters assigned to the blue and green colors. The right image shows an approximated “true” rest-UV color image composed of F200W+F277W in blue, F356W in green, and F410M+F444W in red. As we discuss further in Section 5, intrinsically, this galaxy is quite blue. The scale bar corresponds to 1 (physical) kpc assuming $z = 12$ at a scale of $0''.37 \text{ kpc}^{-1}$.

Python’s astropy package (Bradley et al. 2020). Source detection was performed on a combined F277W and F356W image and the resulting segmentation image passed to the PHOTUTILS SourceCatalog routine, which carried out aperture-matched photometry on the background-subtracted, PSF-matched images in each filter.

The second method is a custom photometry package, where photometry is measured in circular apertures with radii ranging from $0''.10$ to $0''.35$, applying aperture corrections for pointlike sources ($< 0.1 \text{ mag}$ for $r > 0''.25$) and after locally ($30''$ box) aligning the images (Pérez-González et al. 2008). Sky noise measurements in a $6'' \times 6''$ box around the source take into account correlated noise and are used to quote 5σ upper limits for nondetections. Photometric differences for each band are smaller than 0.1 mag for apertures between $0''.2$ and $0''.35$, $0.3\text{--}0.6 \text{ mag}$ fainter for smaller radii, indicating that the source is (slightly) resolved. This method was applied to the non-PSF-matched imaging.

Comparing results between our fiducial SE photometry and these independent methods, we find that both the Lyman break and rest-UV colors show extremely high consistency. The upper limits in F115W are similar to our fiducial values. The F115W – F200W Ly α break color is $> 2.3 \text{ mag}$ (2σ) from the custom method and $> 1.7 \text{ mag}$ (2σ) for PHOTUTILS (compared to $> 1.9 \text{ mag}$ [2σ] for our fiducial SE photometry). Comparing colors, our measured F200W – F444W color of -0.6 ± 0.4 is highly consistent with the measurement from the custom method of -0.7 ± 0.3 . The PHOTUTILS measurement is even bluer (-1.0 ± 0.4) due to a 0.4 mag fainter F444W measurement. We conclude that while differences in photometric packages and associated assumptions (in particular aperture corrections) can affect the photometry at the $\sim 10\%$ – 30% level in most cases, this does not affect the validity of our candidate, as these independent methods find a consistently strong Ly α break followed by a blue spectral slope, fully consistent with our interpretation of a $z \sim 12$ galaxy.

4.2.3. Photometric Redshift Accuracy

Similar to photometry, different photometric redshift packages can also impart biases on results. While we have used a well-tested fiducial package in EAZY and implemented a new set of templates customized for very high redshift galaxies, it is prudent to explore whether other packages would find different photometric redshift results. As we discuss below, we have run the PROSPECTOR (Johnson et al. 2021), BAGPIPES (Carnall et al. 2018), CIGALE (Burgarella et al. 2005; Noll et al. 2009; Boquien et al. 2019), and DENSE BASIS (Iyer & Gawiser 2017; Iyer et al. 2019) SED-fitting codes on our fiducial photometry. While for the stellar population properties discussed below, we use our EAZY-derived $\mathcal{P}(z)$ as a redshift prior, we also performed an independent run with the redshift as a free parameter. Figure 3 shows our fiducial EAZY $\mathcal{P}(z)$ along with the redshift PDFs from these independent runs.

These five results show remarkable consistency, all preferring $z > 12$ with no significant low-redshift solutions. All four codes find results similar to our fiducial EAZY run. PROSPECTOR finds

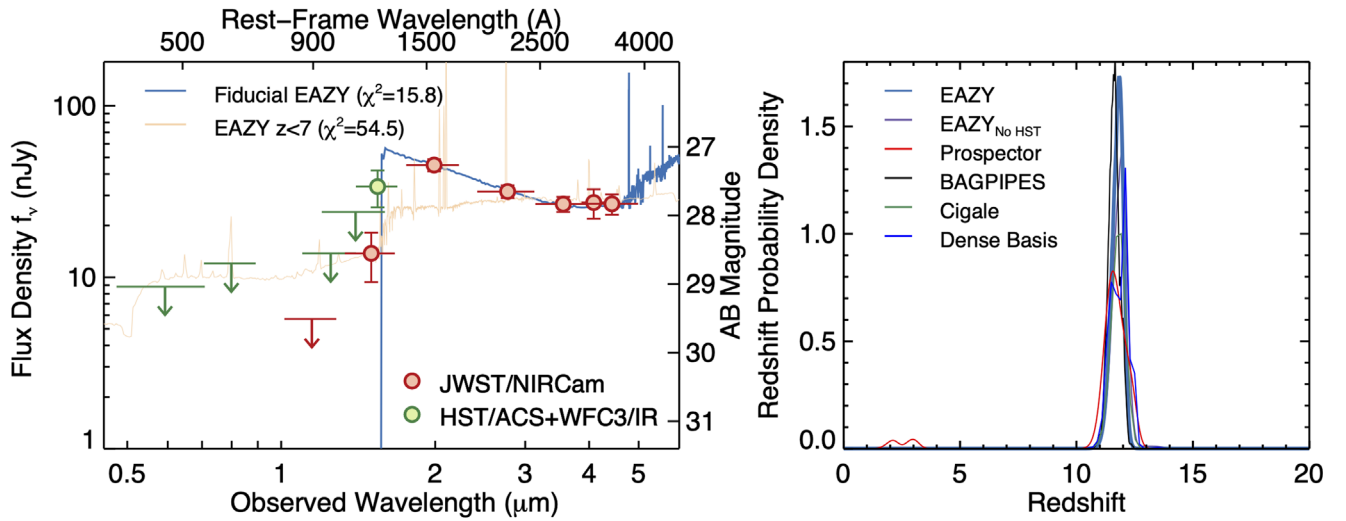


Figure 3. (Left) The circles denote our fiducial photometry, with green and red denoting the HST/ACS+WFC3 and NIRCcam instruments, respectively. This SED exhibits the hallmark shape of a high-redshift galaxy, with several nondetections in blue filters, followed by significant detections with a blue spectral slope. The arrows denote 1σ upper limits. The F115W – F200W break color is >1.9 mag (2σ), which is sufficient to rule out all low-redshift solutions. The blue curve shows the best-fitting EAZY model at $z = 11.8$. The orange curve shows the result if we force EAZY to find a solution at $z < 7$. This model is unable to match the amplitude of the break, as well as the slope redward of the break, and is correspondingly ruled out at high confidence ($\chi^2_{\text{low-}z} = 54.5$ compared to 15.8 for the $z = 11.8$ solution). (Right) Photometric redshift PDFs for Maisie’s Galaxy. The thick blue curve shows the fiducial PDF from EAZY, which exhibits no low-redshift solution and a peak at $z = 11.8^{+0.2}_{-0.3}$ (the purple curve shows the EAZY result without HST photometry, which prefers $z = 12.0$ and has a tail to $z = 14$). The remaining curves show the results from independent runs with PROSPECTOR, BAGPIPES, CIGALE, and DENSE BASIS (see Section 5). All results significantly prefer a $z > 12$ solution, with all four codes finding best-fit redshifts nearly identical to EAZY ($z = 11.8^{+0.2}_{-0.3}$, $11.6^{+0.2}_{-0.2}$, $11.8^{+0.4}_{-0.4}$, and $11.9^{+0.4}_{-0.4}$, respectively).

$z = 11.8^{+0.2}_{-0.3}$, BAGPIPES finds $z = 11.6^{+0.2}_{-0.2}$, CIGALE finds $z = 11.8^{+0.4}_{-0.4}$, and DENSE BASIS finds $z = 11.9^{+0.4}_{-0.4}$. Combining the posteriors of all four photometric redshift estimates provides a redshift PDF in agreement with our fiducial EAZY results with a median redshift of 11.74 and a 97.5% confidence that $z > 11.0$. We conclude that systematic biases due to choices in photometric redshift analyses are not affecting our results. Our fiducial result uses that from EAZY as it used templates trained on observations, while the full grids spanned by the other four codes may include unphysical parameter combinations.

As one final test, we explore the impact of our inclusion of the six additional blue templates in our photometric redshift analysis. Refitting our photometry with the standard templates, we find $z = 11.50^{+0.33}_{-0.33}$, consistent within 1σ of our fiducial result. However, standard templates produce a significantly worse fit ($\chi^2 \sim 34$ versus ~ 15 for the fiducial fit). The standard best-fitting template has an F200W – F277W color of -0.04 mag, while our fiducial template has F200W – F277W = -0.35 ; both can be compared to the observed color of F200W – F277W = -0.39 . It is clear that our inclusion of bluer templates is better able to match the colors of ultrahigh-redshift galaxies such as the one we present here.

4.2.4. Contamination Estimation

To determine the likelihood that our selection criteria would produce a low-redshift contaminant, we imposed our same selection criteria cuts on the simulated catalogs used for all of the mock CEERS observations. We note that there are zero $z > 10$ sources in this catalog, so recovery of any source using these selection criteria would indicate contamination of our high-redshift sample. More information about the simulation used can be found in Yung et al. (2022) and Somerville et al. (2021). We use the perturbed fluxes as described in R. Larson et al. (2022, in preparation), who used the same method as determined by M. Bagley et al. (2022, in preparation), where

they modeled the noise in simulated JWST images to have a Voigt profile distribution. We used the 1σ depth in each filter for our errors and ran the whole catalog through EAZY. As our catalog-level fluxes do not have aperture-specific fluxes, we cannot impose criteria based on those fluxes. We apply the following selection criteria to the simulated catalog: S/N in both F200W and F277W > 6 , $\int \mathcal{P}(z > 8) \geq 0.9$, $z_{\text{best}} > 8.5$, $\chi^2_{\text{eazy}} < 20$, $S/N \leq 1.5$ in F606W, F814W, F115W, F150W, and F200W magnitude < 29 , F200W – F444W color < 1 , and $\chi^2_{\text{Low-}z} - \chi^2_{\text{fiducial}} > 4$. Finally, matching the values to those of Maisie’s Galaxy, which exhibits $S/N > 10$ in both F200W and F277W and $\int \mathcal{P}(z > 11) \geq 0.99$, we find zero sources that meet our criteria. This provides further evidence that Maisie’s Galaxy has a high-redshift nature.

5. Discussion

5.1. Physical Properties

The five photometric detections afforded by NIRCcam allow us the unprecedented opportunity to study the physical properties of a galaxy potentially only ~ 400 Myr after the Big Bang. Our fiducial stellar population modeling is done with the PROSPECTOR Bayesian SED-fitting code (Johnson et al. 2021). We follow the same procedures as in Tacchella et al. (2022), and we refer the reader there for more details. Briefly, we model the SED with a 13-parameter model that includes redshift (where here prior is set to the posterior of EAZY, unlike in Section 4.2.3, where it was free), stellar mass, stellar and gas-phase metallicities, dust attenuation (two-component dust model including birth-cloud dust attenuating young stars (< 10 Myr) and nebular emission, a diffuse component for the whole galaxy with a flexible attenuation law; three parameters), and an ionization parameter for the nebular emission. We adopt a flexible star formation history (SFH) prescription with six time bins (the first two look-back time bins are spaced at 0–5

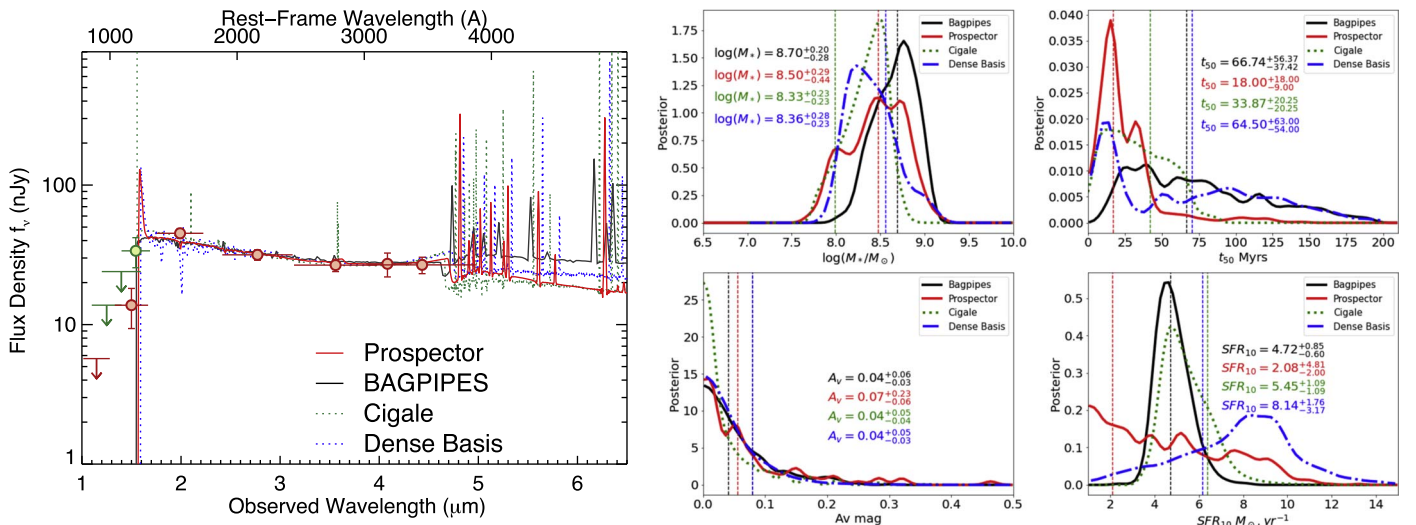


Figure 4. (Left) Our fiducial photometry of Maisie’s Galaxy alongside best-fit SED models from the SED-fitting codes PROSPECTOR (red solid, fiducial; see Table 1), BAGPIPES (black solid), CIGALE (green dotted), and DENSE BASIS (blue dotted). (Right) Posterior distributions of the key stellar population properties from all four codes. The panels show stellar mass, mass-weighted age, dust attenuation, and SFR averaged over the last 10 Myr. The vertical dotted lines indicate the mean of the posteriors. Posteriors of attenuation are consistent between all four codes. PROSPECTOR prefers a younger age than the other three because of a recent burst in the SFH of this object. As a consequence of the burst, PROSPECTOR also estimates a lower SFR. The four estimates of the stellar mass posteriors exhibit significant overlap, though the median values differ by ± 0.2 dex. Future observations in the rest optical with MIRI could break these degeneracies.

and 5–10 Myr, while the other four are log-spaced out to $z=20$; five free parameters) and the bursty continuity prior. Furthermore, we assume the MIST stellar models (Choi et al. 2017) and a Chabrier (2003) initial mass function (IMF).

To explore how robust these properties are, we perform an independent fit with the Bayesian BAGPIPES (Carnall et al. 2018), CIGALE (Burgarella et al. 2005; Noll et al. 2009; Boquien et al. 2019), and DENSE BASIS (Iyer & Gawiser 2017; Iyer et al. 2019) SED-fitting codes. For BAGPIPES, we assumed a simple exponential SFH with a Chabrier IMF and a Calzetti dust attenuation law and included nebular emission with an ionization parameter of 10^{-3} , with Bruzual & Charlot (2003) stellar population models. For CIGALE, we assume a delayed SFH after checking that adding a burst does not significantly modify the results. Bruzual & Charlot (2003) models with a Chabrier IMF and were used. DENSE BASIS was run using the flexible nonparametric SFH model and priors described in Iyer et al. (2019) assuming a Calzetti dust law and a Chabrier IMF. Metallicities in all four codes were allowed to vary to allow the uncertainty in metallicity to be included in the uncertainties on other parameters, though this parameter is not well constrained with photometry alone. We note that PROSPECTOR and CIGALE assume an error floor (of 5% and 10% of the flux, respectively), and that PROSPECTOR, DENSE BASIS, and BAGPIPES always fit the measured fluxes, while CIGALE uses the 1σ uncertainty as both the flux and error when the measured fluxes have $S/N < 1$.

The marginalized posterior values of the inferred physical properties from PROSPECTOR are summarized in Table 1 and Figure 4. We infer a stellar mass of $\log(M_*/M_\odot) = 8.5^{+0.3}_{-0.4}$. The attenuation in this galaxy is rather low, with $A_V = 0.07^{+0.22}_{-0.06}$ mag, though we stress that this is not well constrained because we only fit the rest UV, and it is degenerate with the slope of the attenuation law (which is variable in this fit). However, the low dust attenuation is in agreement with the measured UV spectral slope $\beta = -2.47^{+0.09}_{-0.09}$ (measured using the same techniques as in Tacchella et al. 2022). This blue color implies little dust, though it does not require extremely low metallicities

(e.g., Finkelstein et al. 2012; Dunlop et al. 2013; Bouwens et al. 2014). Interestingly, this galaxy is about as blue as $z \sim 7$ galaxies of similar mass (Finkelstein et al. 2012), implying little evolution in chemical enrichment between these two epochs for similar-mass galaxies.

We infer an SFR_{10} (average of the past 10 Myr¹⁰⁰) of $2.1 M_\odot \text{ yr}^{-1}$, and the corresponding $sSFR_{10}$ is $10^{-8.2} \text{ yr}^{-1}$. By looking at the posterior distribution of the SFH, it becomes apparent that the model for this galaxy had an episode of elevated star formation 10–20 Myr ago with an SFR of $8^{+17}_{-7} M_\odot \text{ yr}^{-1}$; i.e., the SFR has been slightly decreasing in the recent 10 Myr. This explains the mass-weighted age of 18^{+18}_{-9} Myr. This is also consistent with the half-mass formation time of dark matter halos at $z \sim 12$ of a few tens of megayears (Tacchella et al. 2018).

These PROSPECTOR-based posterior distributions are consistent with the ones from BAGPIPES, CIGALE, and DENSE BASIS (see Figure 4), though the difference in age is large (age is defined at half-mass time, t_{50} , which is close to the mass-weighted age). BAGPIPES, CIGALE, and DENSE BASIS prefer higher age values (although the posterior distributions are also broader) of 67^{+56}_{-37} , 34 ± 20 , and 64^{+63}_{-54} Myr, respectively. The SFH inferred from DENSE BASIS shows a recent burst of star formation in the last ~ 30 Myr. The larger mass-weighted age comes from the long tail of low-level star formation in the galaxy leading up to the recent burst. The spread in these results could be explained by differences in SFHs (e.g., nonparametric versus parametric), as well as the lack of observational constraints in the rest-frame optical. These differences also lead to PROSPECTOR having the lowest SFR_{10} value.

Several pre-JWST studies have focused on inferring SFHs and stellar ages of $z \approx 8$ –10 galaxies (e.g., Hashimoto et al. 2018; Laporte et al. 2021; Stefanon et al. 2022). Specifically,

¹⁰⁰ Although the SFR_{10} would be best estimated from nebular emission lines, the (F)UV actually also probes such short timescales, in particular for the bursty star formation (e.g., Caplar & Tacchella 2019; Flores Velázquez et al. 2021) expected at these redshifts.

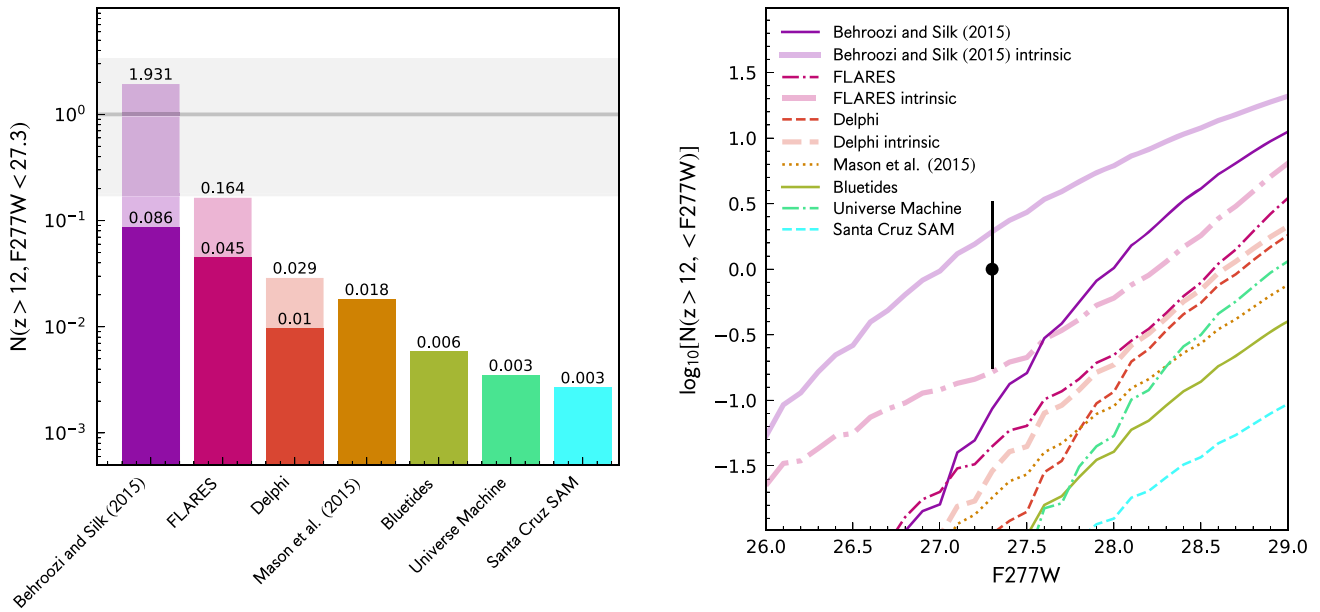


Figure 5. Theoretical predictions from a range of simulations in the recent literature. The left panel shows the predicted number of sources at $m < 27.3$ (the brightness of our source) and $z > 12$ over our survey area of 34.5 arcmin^2 . The vertical axis and the values above each bar give the number predicted. Dark (light) shading denotes the value derived from models with (without) dust attenuation applied. The right panel shows the same theoretical predictions, now showing the cumulative number as a function of apparent magnitude. The bulk of these models predict that $m \sim 27$ galaxies at $z \gtrsim 12$ are not highly likely, though the Behroozi & Silk (2015) model, which has no accelerated decline in the cosmic SFR density at $z > 8$, has the least tension. However, our detection of one source has a large Poisson (and cosmic variance) uncertainty (gray shading in the left panel; error bar in the right), so strong conclusions cannot yet be made.

Tacchella et al. (2022)—using PROSPECTOR with the same bursty continuity prior—found a diversity of stellar ages, ranging from 10 to 260 Myr, and stellar masses (10^9 – $10^{11} M_\odot$), with more massive galaxies being older. In particular, the galaxies at $z \approx 9$ –10 with stellar masses at the higher end and older ages ($t_{50} \approx 100$ Myr) are consistent with being the descendants of Maisie’s Galaxy. Recently, Naidu et al. (2022) inferred the properties of two galaxies at $z \approx 10.6$ and 12.4 (see also Castellano et al. 2022) with PROSPECTOR and a similar setup, allowing us to do a useful comparison. Their two galaxies have $\log(M_*/M_\odot) = 9.4^{+0.3}_{-0.3}$ and $9.0^{+0.3}_{-0.4}$, $\text{SFR}_{50\text{Myr}} = 12^{+9}_{-4}$ and $7^{+4}_{-3} M_\odot \text{ yr}^{-1}$, and $t_{50} = 111^{+43}_{-54}$ and 71^{+33}_{-32} Myr, respectively. This is older than what we infer for our galaxy, though this age difference could be explained by the stellar mass difference, along with the higher preferred redshift for Maisie’s Galaxy. Importantly, detailed stellar population analyses of early galaxies will advance significantly with JWST, particularly when including spectroscopic information.

5.2. Source Morphology

We derive the size of Maisie’s Galaxy using two morphological fitting codes, GALFITM¹⁰¹ (Häußler et al. 2013) and STATMORPH¹⁰² (Rodríguez-Gomez et al. 2019). GALFITM is a modified version of GALFIT¹⁰³ (Peng et al. 2002, 2010), a least-squares fitting algorithm that finds the optimum Sérsic fit to a galaxy’s light profile. We perform fits using GALFITM by allowing the Sérsic index to vary between 0.01 and 8, the magnitude of the galaxy between 0 and 45, and r_{half} between 0.3 and 200 pixels (on our $0''.03$ pixel scale). As input, we use a 100×100 pixel cutout of the F277W science

image, the segmentation map created by SE, and the empirical PSF measured from our CEERS2 pointing, which we allow GALFITM to oversample relative to the data by a factor of 9. We estimate the uncertainty on our fits by conducting a Monte Carlo analysis where we modify the input F277W science image to randomly vary the pixel-to-pixel noise, recompute the parameters, and then repeat this analysis 40 times.

Following this procedure, we measure a half-light radius of 3.0 ± 0.12 pixels ($0''.09 \pm 0''.0036$), which corresponds to a physical size of 340 ± 14 pc at $z = 11.8$. We check these results using the standard configuration of STATMORPH, a Python package developed to calculate the nonparametric morphology of galaxies, as well as compute single Sérsic fits. Using the same images as input, we find a half-light radius of 2.9 pixels, in good agreement with the measurement from GALFITM. We repeat this measurement for the F200W filter and a stacked F200W + F277W image and find consistent results. The measured half-light radius of 3.0 ± 0.1 pixels is significantly larger than that expected for a point source (the median r_h for our PSF stars is 1.95 ± 0.22 pixels in F277W), further ruling out a stellar origin for this source.

5.3. Comparison to Model Predictions

In Figure 5, we present predictions from a range of theoretical models: the First Light And Reionisation Epoch Simulations (FLARES; Lovell et al. 2021; Vijayan et al. 2021; Wilkins et al. 2022), a suite of hydrodynamical cosmological zoom simulations; the large periodic volume hydrodynamical simulation Bluetides (Feng et al. 2016; Wilkins et al. 2017); the Delphi (Dayal et al. 2014, 2022) and Santa Cruz (Yung et al. 2019, 2020) semianalytical models; the semiempirical UNIVERSEMACHINE (Behroozi et al. 2020), Mason et al. (2015); and Behroozi & Silk (2015) models. For the FLARES, Delphi, and Behroozi & Silk (2015) models, we show both the

¹⁰¹ <https://www.nottingham.ac.uk/astronomy/megamorph/>

¹⁰² <https://statmorph.readthedocs.io/en/latest/>

¹⁰³ <https://users.obs.carnegiescience.edu/peng/work/galfit/galfit.html>

attenuated and unattenuated (intrinsic) predictions. These predictions were made by interpolating and integrating either the binned or Schechter luminosity functions across $z = 15 \rightarrow 12$, taking account of the areal size of the CEERS observations. Almost all of these models predict an expected source density much less than 1, making the observation of even a single object at this redshift and magnitude surprising and potentially hinting at significant differences between the physical assumptions in these models and the real early universe.

The exception is the Behroozi & Silk (2015) model, which extrapolated galaxy formation to high redshifts by assuming that the ratio between galaxies' sSFRs and their host halos' specific accretion rates remained constant, which they showed was equivalent to assuming that galaxies' stellar masses are proportional to a power of their host halo masses. This model was constrained only with observational data at $z \leq 8$ and predicted no change in the slope of the CSFR relation with redshift at $z > 8$. As a result, it predicted many more high-redshift galaxies than later models that were constrained to match $z \sim 9$ and ~ 10 data from HST that suggested more rapid declines in the number densities of early galaxies. We caution against overinterpretation, as the current sample contains only a single object with a consequently large Poisson error in addition to additional uncertainty due to cosmic variance. Nevertheless, if confirmed, the existence of this object places informative constraints on galaxy formation models in this epoch.

5.4. Comparisons to Extrapolations from Lower Redshift

We are now only just getting our first glimpse into this epoch with the first JWST data. Nonetheless, we can compare our observed number density to a few recent observations. We calculate a rough number density for $M_{UV} = -20.3$ galaxies assuming a top-hat selection function over $11.5 < z < 12.5$. This is overly simplistic and does not account for incompleteness (which, although this is a $>10\sigma$ detection, certainly is nonunity due to our stringent selection criteria). Nonetheless, it is illustrative of a rough number density. We find a maximum volume over the CEERS first-epoch area of $5.0 \times 10^4 \text{ Mpc}^3$ for a number density for our singular source of $2.0_{-1.7}^{+4.6} \times 10^{-5} \text{ Mpc}^{-3}$ (where the uncertainties are Poisson based on our detection of one object).

We illustrate this number density in Figure 6. Our derived number density is not inconsistent with a variety of observational constraints at $z \sim 10$, as well as recent results at $z \sim 12$ –13. The solid gray line shows the predicted $z = 12$ Schechter function from Finkelstein (2016), which is extrapolated from an empirical fit to observations at $z = 4$ –8, assuming smooth redshift evolution. Interestingly, our rough number density measurement is above this prediction, though consistent within the 1σ uncertainties, which would support its assumption of a smooth decline in the luminosity function (and the corresponding SFRD). Our results are also consistent with the smoothly evolving double power-law (DPL) model at $z = 12$ from Finkelstein & Bagley (2022), again supporting a smooth decline in the rest-UV luminosity function to $z > 10$.

As noted by several previous studies, the bright end of the luminosity function at $z \geq 9$ exhibits an interesting excess over predicted levels (e.g., Morishita et al. 2018; Bowler et al. 2020; Rojas-Ruiz et al. 2020; Bagley et al. 2022; Finkelstein et al. 2022). While our survey area does not yet probe the volume densities needed to reach these brighter potential $z = 12$ galaxies, if the high-

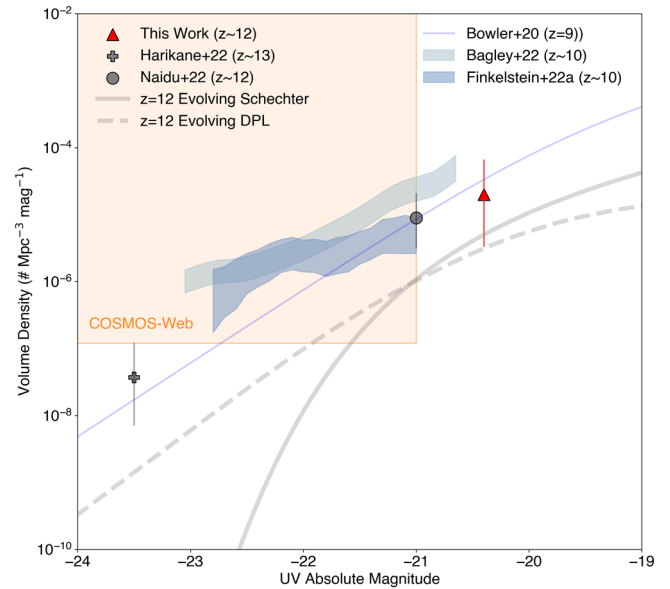


Figure 6. View of the luminosity function at $z \geq 10$. The shaded light blue regions show observational constraints at $z \sim 10$ (Bagley et al. 2022; Finkelstein et al. 2022), while the thin line shows the $z = 9$ DPL luminosity function from Bowler et al. (2020). The remaining points show $z > 12$ results from this work (triangle), the ground-based work of Harikane et al. (2022), and the recent JWST work of Naidu et al. (2022). The thick lines show empirical luminosity function models that evolve smoothly with redshift, with the solid line denoting a Schechter function evolved to $z = 12$ (Finkelstein 2016) and the dashed line a DPL evolved to $z = 12$ (Finkelstein & Bagley 2022). The constraints placed by our observations on the faint end of the luminosity function are consistent with a smooth decline out to $z \sim 12$, though both our observations and those of brighter galaxies do lie above the bright extension of these smoothly declining functions. The shaded box shows the parameter space reached by the upcoming COSMOS-Web survey, which will probe the very bright end at these redshifts.

redshift luminosity function follows a DPL form, the forthcoming 0.6 deg^2 COSMOS-Web survey (PIs: Kartaltepe & Casey) should be able to discover this population. In combination with the full Cycle 1 slate of surveys, including the completed CEERS imaging, it will afford a more complete view of the $z = 12$ universe.

6. Conclusions

We present the results from a search for ultrahigh-redshift galaxy candidates from the first epoch of NIRCcam imaging from the JWST CEERS survey. We use imaging from both the SW and LW cameras over four pointings covering 34.5 arcmin^2 in the F115W, F150W, F200W, F277W, F356W, F410W, and F444W filters, reaching $m \sim 29$ (5σ) in the deepest bands. We measure photometry using SE, with an emphasis on robust measurements of colors, total fluxes, and uncertainties.

We estimate photometric redshifts with the EAZY software package, including new blue templates designed to better recover the colors of very distant galaxies. We iteratively develop a set of conservative selection criteria to select candidate galaxies at $z \geq 12$. We find one candidate galaxy satisfying stringent nondetections ($S/N < 1.5$) in all dropout bands and detected at $>10\sigma$ in the detection bands.

This object, dubbed Maisie's Galaxy, has a photometric redshift of $11.8_{-0.3}^{+0.2}$ and was found in the CEERS2 field. We explored all known potential sources of contamination, including instrumental effects, systematic biases in the analysis, and contamination by lower-redshift galaxies or Galactic stars.

We find that none of these alternative explanations can account for the observations, leaving us with the conclusion that it is a robust $z \sim 12$ galaxy candidate.

We explore the physical properties of this unexpected galaxy. As might be expected for such an early epoch, this galaxy is blue, with a UV spectral slope $\beta = -2.5$, consistent with low levels of dust attenuation. Stellar population models with multiple codes are in agreement that this source has a modest stellar mass of $\log(M/M_\odot) \sim 8.5$, with a high \log sSFR of -8.2 yr^{-1} . The mass-weighted age of Maisie’s Galaxy is young, with a median of ~ 20 Myr, though stellar populations as old as 100 Myr ($z_{\text{form}} \geq 14$) cannot be ruled out. The galaxy candidate is significantly resolved, with $r_h = 3.0 \pm 0.1$ pixels, for a physical size of ~ 340 pc at $z \approx 12$.

We compare the abundance of this single galaxy to both model predictions and previous observations. We find that the presence of this source is unexpected based on most model predictions, though given our sample size, the tension is modest at best. However, both semiempirical models and empirical extrapolations that assume a smooth decline in the SFR density at $z > 8$ predict volume densities of such $z \sim 12$ sources in agreement with our observations. Should more such sources be found in early JWST surveys, it would provide further evidence against accelerated-decline SFR density scenarios.

Such a galaxy population would also present challenges for a variety of dark matter models with suppressed power on small scales, such as fuzzy dark matter (e.g., Sullivan et al. 2018), and possibly even for standard Λ CDM models. Additionally, the presence of this galaxy ~ 370 Myr after the Big Bang may be consistent with redshifted 21 cm absorption at $z \sim 18$ reported by the Experiment to Detect the Global Epoch of Reionization Signature (EDGES; Bowman et al. 2018) presumed to be caused by light from the first stars.

We caution the reader that this galaxy is a candidate. While we have exhausted multiple avenues to explore whether its presence in our data could be caused by instrumental effects, our measurement techniques were biased, or its colors could be consistent with lower-redshift sources, the “gold standard” of distance measurements is spectroscopic confirmation. Such confirmation should be possible in modest exposure times with the NIRSpec and/or MIRI spectrographs on board JWST. The combination of larger samples being compiled by JWST Cycle 1 programs, including the remainder of CEERS, COSMOS-Web (PIs: Kartaltepe & Casey), JADES (PIs: Rieke & Ferruit), PRIMER (PI: Dunlop), PEARLS (R. Windhorst et al. 2022, in preparation), and NGDEEP (PIs: Finkelstein, Papovich, & Pirzkal), coupled with subsequent spectroscopic follow-up, will further illuminate the earliest phases of galaxy formation.

We acknowledge that the location where this work took place, the University of Texas at Austin, sits on indigenous land. The Tonkawa lived in central Texas, and the Comanche and Apache moved through this area. We pay our respects to all of the American Indian and Indigenous Peoples and communities who have been or have become a part of these lands and territories in Texas on this piece of Turtle Island.

We thank the entire JWST team, including the engineers, for making possible this wonderful overperforming telescope, the commissioning team for obtaining these early data, and the pipeline teams for their work over the years building and supporting the pipeline. The authors acknowledge the Texas

Advanced Computing Center (TACC) at the University of Texas at Austin for providing HPC and visualization resources that have contributed to the research results reported within this paper. We thank Brendan Bowler, Caroline Morley, Jim Dunlop, and Mike Boylan-Kolchin for helpful conversations and the anonymous referee for constructive comments.

We acknowledge support from NASA through STScI ERS award JWST-ERS-1345. D.B. and M.H.-C. thank the Programme National de Cosmologie et Galaxies and CNES for their support. R.A. acknowledges support from Fondecyt Regular 1202007.

Software: Astropy (Astropy Collaboration et al. 2013), BAGPIPES (Carnall et al. 2018), CIGALE (Burgarella et al. 2005; Noll et al. 2009; Boquien et al. 2019), DENSE BASIS (Iyer & Gawiser 2017; Iyer et al. 2019), Drizzle (Fruchter & Hook 2002), EAZY (Brammer et al. 2008), GALFITM (Peng et al. 2010; Häußler et al. 2013), PHOTUTILS (Bradley et al. 2020), PROSPECTOR (Johnson et al. 2021), SciPy (Virtanen et al. 2020), SEXTRACTOR (Bertin & Arnouts 1996), STATMORPH (Rodríguez-Gomez et al. 2019), STScI JWST Calibration Pipeline (jwst-pipeline.readthedocs.io).

ORCID iDs

Steven L. Finkelstein  <https://orcid.org/0000-0001-8519-1130>
Micaela B. Bagley  <https://orcid.org/0000-0002-9921-9218>
Pablo Arrabal Haro  <https://orcid.org/0000-0002-7959-8783>
Mark Dickinson  <https://orcid.org/0000-0001-5414-5131>
Henry C. Ferguson  <https://orcid.org/0000-0001-7113-2738>
Jeyhan S. Kartaltepe  <https://orcid.org/0000-0001-9187-3605>
Casey Papovich  <https://orcid.org/0000-0001-7503-8482>
Denis Burgarella  <https://orcid.org/0000-0002-4193-2539>
Dale D. Kocevski  <https://orcid.org/0000-0002-8360-3880>
Marc Huertas-Company  <https://orcid.org/0000-0002-1416-8483>
Karthik G. Iyer  <https://orcid.org/0000-0001-9298-3523>
Anton M. Koekemoer  <https://orcid.org/0000-0002-6610-2048>
Rebecca L. Larson  <https://orcid.org/0000-0003-2366-8858>
Pablo G. Pérez-González  <https://orcid.org/0000-0003-4528-5639>
Caitlin Rose  <https://orcid.org/0000-0002-8018-3219>
Sandro Tacchella  <https://orcid.org/0000-0002-8224-4505>
Stephen M. Wilkins  <https://orcid.org/0000-0003-3903-6935>
Katherine Chworowsky  <https://orcid.org/0000-0003-4922-0613>
Alexa M. Morales  <https://orcid.org/0000-0003-4965-0402>
Rachel S. Somerville  <https://orcid.org/0000-0002-6748-6821>
L. Y. Aaron Yung  <https://orcid.org/0000-0003-3466-035X>
Adriano Fontana  <https://orcid.org/0000-0003-3820-2823>
Mauro Giavalisco  <https://orcid.org/0000-0002-7831-8751>
Andrea Grazian  <https://orcid.org/0000-0002-5688-0663>
Norman A. Grogin  <https://orcid.org/0000-0001-9440-8872>
Lisa J. Kewley  <https://orcid.org/0000-0001-8152-3943>
Allison Kirkpatrick  <https://orcid.org/0000-0002-1306-1545>
Peter Kurczynski  <https://orcid.org/0000-0002-8816-5146>
Jennifer M. Lotz  <https://orcid.org/0000-0003-3130-5643>
Laura Pentericci  <https://orcid.org/0000-0001-8940-6768>
Nor Pirzkal  <https://orcid.org/0000-0003-3382-5941>
Swara Ravindranath  <https://orcid.org/0000-0002-5269-6527>

Russell E. Ryan, Jr. <https://orcid.org/0000-0003-0894-1588>
 Jonathan R. Trump <https://orcid.org/0000-0002-1410-0470>
 Guang Yang <https://orcid.org/0000-0001-8835-7722>
 Omar Almaini <https://orcid.org/0000-0001-9328-3991>
 Ricardo O. Amorín <https://orcid.org/0000-0001-5758-1000>
 Marianna Annunziatella <https://orcid.org/0000-0002-8053-8040>
 Bren E. Backhaus <https://orcid.org/0000-0001-8534-7502>
 Peter Behroozi <https://orcid.org/0000-0002-2517-6446>
 Eric F. Bell <https://orcid.org/0000-0002-5564-9873>
 Rachana Bhatawdekar <https://orcid.org/0000-0003-0883-2226>
 Laura Bisigello <https://orcid.org/0000-0003-0492-4924>
 Volker Bromm <https://orcid.org/0000-0003-0212-2979>
 Véronique Buat <https://orcid.org/0000-0003-3441-903X>
 Fernando Buitrago <https://orcid.org/0000-0002-2861-9812>
 Antonello Calabrò <https://orcid.org/0000-0003-2536-1614>
 Caitlin M. Casey <https://orcid.org/0000-0002-0930-6466>
 Marco Castellano <https://orcid.org/0000-0001-9875-8263>
 Óscar A. Chávez Ortiz <https://orcid.org/0000-0003-2332-5505>
 Laure Ciesla <https://orcid.org/0000-0003-0541-2891>
 Nikko J. Cleri <https://orcid.org/0000-0001-7151-009X>
 Seth H. Cohen <https://orcid.org/0000-0003-3329-1337>
 Justin W. Cole <https://orcid.org/0000-0002-6348-1900>
 Kevin C. Cooke <https://orcid.org/0000-0002-2200-9845>
 M. C. Cooper <https://orcid.org/0000-0003-1371-6019>
 Asantha R. Cooray <https://orcid.org/0000-0002-3892-0190>
 Luca Costantin <https://orcid.org/0000-0001-6820-0015>
 Isabella G. Cox <https://orcid.org/0000-0002-1803-794X>
 Darren Croton <https://orcid.org/0000-0002-5009-512X>
 Emanuele Daddi <https://orcid.org/0000-0002-3331-9590>
 Romeel Davé <https://orcid.org/0000-0003-2842-9434>
 Alexander de la Vega <https://orcid.org/0000-0002-6219-5558>
 Avishai Dekel <https://orcid.org/0000-0003-4174-0374>
 David Elbaz <https://orcid.org/0000-0002-7631-647X>
 Vicente Estrada-Carpenter <https://orcid.org/0000-0001-8489-2349>
 Vital Fernández <https://orcid.org/0000-0003-0531-5450>
 Keely D. Finkelstein <https://orcid.org/0000-0003-0792-5877>
 Jonathan Freundlich <https://orcid.org/0000-0002-5245-7796>
 Seiji Fujimoto <https://orcid.org/0000-0001-7201-5066>
 Ángela García-Argumánuez <https://orcid.org/0000-0002-8365-5525>
 Jonathan P. Gardner <https://orcid.org/0000-0003-2098-9568>
 Eric Gawiser <https://orcid.org/0000-0003-1530-8713>
 Carlos Gómez-Guijarro <https://orcid.org/0000-0002-4085-9165>
 Yuchen Guo <https://orcid.org/0000-0002-4162-6523>
 Kurt Hamblin <https://orcid.org/0000-0002-6292-4589>
 Timothy S. Hamilton <https://orcid.org/0000-0002-9753-1769>
 Nimish P. Hathi <https://orcid.org/0000-0001-6145-5090>
 Benne W. Holwerda <https://orcid.org/0000-0002-4884-6756>
 Michaela Hirschmann <https://orcid.org/0000-0002-3301-3321>
 Taylor A. Hutchison <https://orcid.org/0000-0001-6251-4988>
 Anne E. Jaskot <https://orcid.org/0000-0002-6790-5125>
 Saurabh W. Jha <https://orcid.org/0000-0001-8738-6011>
 Shardha Jogee <https://orcid.org/0000-0002-1590-0568>
 Stéphanie Juneau <https://orcid.org/0000-0002-0000-2394>
 Intae Jung <https://orcid.org/0000-0003-1187-4240>

Susan A. Kassin <https://orcid.org/0000-0002-3838-8093>
 Aurélien Le Bail <https://orcid.org/0000-0002-9466-2763>
 Gene C. K. Leung <https://orcid.org/0000-0002-9393-6507>
 Ray A. Lucas <https://orcid.org/0000-0003-1581-7825>
 Benjamin Magnelli <https://orcid.org/0000-0002-6777-6490>
 Jasleen Matharu <https://orcid.org/0000-0002-7547-3385>
 Elizabeth J. McGrath <https://orcid.org/0000-0001-8688-2443>
 Emiliano Merlin <https://orcid.org/0000-0001-6870-8900>
 Jeffrey A. Newman <https://orcid.org/0000-0001-8684-2222>
 David C. Nicholls <https://orcid.org/0000-0003-0892-5203>
 Viraj Pandya <https://orcid.org/0000-0002-2499-9205>
 Marc Rafelski <https://orcid.org/0000-0002-9946-4731>
 Kaila Ronayne <https://orcid.org/0000-0001-5749-5452>
 Paola Santini <https://orcid.org/0000-0002-9334-8705>
 Lise-Marie Seillé <https://orcid.org/0000-0001-7755-4755>
 Ekta A. Shah <https://orcid.org/0000-0001-7811-9042>
 Lu Shen <https://orcid.org/0000-0001-9495-7759>
 Raymond C. Simons <https://orcid.org/0000-0002-6386-7299>
 Gregory F. Snyder <https://orcid.org/0000-0002-4226-304X>
 Elizabeth R. Stanway <https://orcid.org/0000-0002-8170-809X>
 Amber N. Straughn <https://orcid.org/0000-0002-4772-7878>
 Harry I. Teplitz <https://orcid.org/0000-0002-7064-5424>
 Brittany N. Vanderhoof <https://orcid.org/0000-0002-8163-0172>
 Jesús Vega-Ferrero <https://orcid.org/0000-0003-2338-5567>
 Weichen Wang <https://orcid.org/0000-0002-9593-8274>
 Benjamin J. Weiner <https://orcid.org/0000-0001-6065-7483>
 Christopher N. A. Willmer <https://orcid.org/0000-0001-9262-9997>
 Stijn Wuyts <https://orcid.org/0000-0003-3735-1931>

References

- Astropy Collaboration, Robitaille, T. P., Tollerud, E. J., et al. 2013, *A&A*, 558, A33
- Bagley, M. B., Finkelstein, S. L., Rojas-Ruiz, S., et al. 2022, arXiv:2205.12980
- Behroozi, P., Conroy, C., Wechsler, R. H., et al. 2020, *MNRAS*, 499, 5702
- Behroozi, P. S., & Silk, J. 2015, *ApJ*, 799, 32
- Bertin, E., & Arnouts, S. 1996, *A&AS*, 117, 393
- Boquien, M., Burgarella, D., Roehly, Y., et al. 2019, *A&A*, 622, A103
- Bouwens, R. J., Illingworth, G. D., Oesch, P. A., et al. 2014, *ApJ*, 793, 115
- Bouwens, R. J., Illingworth, G. D., Oesch, P. A., et al. 2015, *ApJ*, 803, 34
- Bouwens, R. J., Oesch, P. A., Stefanon, M., et al. 2021, *AJ*, 162, 47
- Bowler, R. A. A., Jarvis, M. J., Dunlop, J. S., et al. 2020, *MNRAS*, 493, 2059
- Bowman, J. D., Rogers, A. E. E., Monsalve, R. A., Mozdzen, T. J., & Mahesh, N. 2018, *Natur*, 555, 67
- Bradley, L., Sipőcz, B., Robitaille, T., et al. 2020, astropy/photutils: v1.0.0, Zenodo, doi:10.5281/zenodo.4044744
- Brammer, G. B., van Dokkum, P. G., & Coppi, P. 2008, *ApJ*, 686, 1503
- Bruzual, G., & Charlot, S. 2003, *MNRAS*, 344, 1000
- Burgarella, D., Buat, V., & Iglesias-Paramo, J. 2005, *MNRAS*, 360, 1413
- Burgasser, A. J. 2014, in Int. Workshop on Stellar Spectral Libraries ASI Conf. Ser., The SpeX Prism Library: 1000+ low-resolution, near-infrared spectra of ultracool M, L, T and Y dwarfs, 11, ed. H. P. Singh, P. Prugniel, & I. Vauglin (New York: Plenum), 7
- Caballero, J. A., Burgasser, A. J., & Klement, R. 2008, *A&A*, 488, 181
- Caplar, N., & Tacchella, S. 2019, *MNRAS*, 487, 3845
- Cardelli, J. A., Clayton, G. C., & Mathis, J. S. 1989, *ApJ*, 345, 245
- Carnall, A. C., McLure, R. J., Dunlop, J. S., & Dave, R. 2018, *MNRAS*, 480, 4379
- Casertano, S., de Mello, D., Dickinson, M., et al. 2000, *AJ*, 120, 2747
- Casey, C. M., Scoville, N. Z., Sanders, D. B., et al. 2014, *ApJ*, 796, 95
- Castellano, M., Fontana, A., Treu, T., et al. 2022, *ApJL*, 938, L15
- Chabrier, G. 2003, *PASP*, 115, 763
- Choi, J., Conroy, C., & Byler, N. 2017, *ApJ*, 838, 159
- Coe, D., Zitrin, A., Carrasco, M., et al. 2013, *ApJ*, 762, 32

- Conroy, C., & Gunn, J. E. 2010, FSPS: Flexible Stellar Population Synthesis, Astrophysics Source Code Library, ascl:1010.043
- Dayal, P., & Ferrara, A. 2018, *PhR*, 780, 1
- Dayal, P., Ferrara, A., Dunlop, J. S., & Pacucci, F. 2014, *MNRAS*, 445, 2545
- Dayal, P., Ferrara, A., Sommovigo, L., et al. 2022, *MNRAS*, 512, 989
- Dunlop, J. S., Rogers, A. B., McLure, R. J., et al. 2013, *MNRAS*, 432, 3520
- Eldridge, J. J., & Stanway, E. R. 2009, *MNRAS*, 400, 1019
- Feng, Y., Di-Matteo, T., Croft, R. A., et al. 2016, *MNRAS*, 455, 2778
- Ferland, G. J., Korista, K. T., Verner, D. A., et al. 1998, *PASP*, 110, 761
- Finkelstein, S. L. 2016, *PASA*, 33, e037
- Finkelstein, S. L., Bagley, M., Song, M., et al. 2022, *ApJ*, 928, 52
- Finkelstein, S. L., & Bagley, M. B. 2022, *ApJ*, 938, 25
- Finkelstein, S. L., Papovich, C., Salmon, B., et al. 2012, *ApJ*, 756, 164
- Finkelstein, S. L., Ryan, R. E., Jr., Papovich, C., et al. 2015, *ApJ*, 810, 71
- Flores Velazquez, J. A., Gurvich, A. B., Faucher-Giguère, C.-A., et al. 2021, *MNRAS*, 501, 4812
- Fruchter, A. S., & Hook, R. N. 2002, *PASP*, 114, 144
- Geach, J. E., Dunlop, J. S., Halpern, M., et al. 2017, *MNRAS*, 465, 1789
- Gnedin, N. Y. 2016, *ApJL*, 825, L17
- Greene, T. P., Chu, L., Egami, E., et al. 2016, *Proc. SPIE*, 9904, 99040E
- Grogin, N. A., Kocevski, D. D., Faber, S. M., et al. 2011, *ApJS*, 197, 35
- Hainline, K. N., Hviding, R. E., Rieke, M., et al. 2020, *ApJ*, 892, 125
- Harikane, Y., Inoue, A. K., Mawatari, K., et al. 2022, *ApJ*, 929, 1
- Hashimoto, T., Laporte, N., Mawatari, K., et al. 2018, *Natur*, 557, 392
- Häußler, B., Bamford, S. P., Vika, M., et al. 2013, *MNRAS*, 430, 330
- Iyer, K., & Gawiser, E. 2017, *ApJ*, 838, 127
- Iyer, K. G., Gawiser, E., Faber, S. M., et al. 2019, *ApJ*, 879, 116
- Jakobsen, P., Ferruit, P., Alves de Oliveira, C., et al. 2022, *A&A*, 661, A80
- Jiang, L., Kashikawa, N., Wang, S., et al. 2021, *NatAs*, 5, 256
- Johnson, B. D., Leja, J., Conroy, C., & Speagle, J. S. 2021, *ApJS*, 254, 22
- Koekemoer, A. M., Faber, S. M., Ferguson, H. C., et al. 2011, *ApJS*, 197, 36
- Laporte, N., Meyer, R. A., Ellis, R. S., et al. 2021, *MNRAS*, 505, 3336
- Lovell, C. C., Vijayan, A. P., Thomas, P. A., et al. 2021, *MNRAS*, 500, 2127
- Lutz, D., Poglitsch, A., Altieri, B., et al. 2011, *A&A*, 532, A90
- Madau, P., & Dickinson, M. 2014, *ARA&A*, 52, 415
- Magnelli, B., Elbaz, D., Chary, R. R., et al. 2009, *A&A*, 496, 57
- Mason, C. A., Trenti, M., & Treu, T. 2015, *ApJ*, 813, 21
- McLeod, D. J., McLure, R. J., & Dunlop, J. S. 2016, *MNRAS*, 459, 3812
- Morishita, T., Trenti, M., Stiavelli, M., et al. 2018, *ApJ*, 867, 150
- Naidu, R. P., Oesch, P. A., van Dokkum, P., et al. 2022, arXiv:2207.09434
- Noll, S., Burgarella, D., Giovannoli, E., et al. 2009, *A&A*, 507, 1793
- Oesch, P. A., Bouwens, R. J., Illingworth, G. D., Labbé, I., & Stefanon, M. 2018, *ApJ*, 855, 105
- Oesch, P. A., Brammer, G., van Dokkum, P. G., et al. 2016, *ApJ*, 819, 129
- Oke, J. B., & Gunn, J. E. 1983, *ApJ*, 266, 713
- Oliver, S. J., Bock, J., Altieri, B., et al. 2012, *MNRAS*, 424, 1614
- Papovich, C., Shipley, H. V., Mehrrens, N., et al. 2016, *ApJS*, 224, 28
- Patten, B. M., Stauffer, J. R., Burrows, A., et al. 2006, *ApJ*, 651, 502
- Peng, C. Y., Ho, L. C., Impey, C. D., & Rix, H.-W. 2002, *AJ*, 124, 266
- Peng, C. Y., Ho, L. C., Impey, C. D., & Rix, H.-W. 2010, *AJ*, 139, 2097
- Pérez-González, P. G., Rieke, G. H., Villar, V., et al. 2008, *ApJ*, 675, 234
- Planck Collaboration, Aghanim, N., Akrami, Y., et al. 2020, *A&A*, 641, A6
- Rieke, G. H., Wright, G. S., Böker, T., et al. 2015, *PASP*, 127, 584
- Rieke, M. J., Kelly, D., & Horner, S. 2005, *Proc. SPIE*, 5904, 1
- Robertson, B. E. 2022, *ARA&A*, 60, 121
- Rodríguez-Gomez, V., Snyder, G. F., Lotz, J. M., et al. 2019, *MNRAS*, 483, 4140
- Rojas-Ruiz, S., Finkelstein, S. L., Bagley, M. B., et al. 2020, *ApJ*, 891, 146
- Ryan, R. E. J., Hathi, N. P., Cohen, S. H., & Windhorst, R. A. 2005, *ApJL*, 631, L159
- Schlawin, E., Leisenring, J., Misselt, K., et al. 2020, *AJ*, 160, 231
- Skelton, R. E., Whitaker, K. E., Momcheva, I. G., et al. 2014, *ApJS*, 214, 24
- Somerville, R. S., Olsen, C., Yung, L. Y. A., et al. 2021, *MNRAS*, 502, 4858
- Stark, D. P. 2016, *ARA&A*, 54, 761
- Stefanon, M., Bouwens, R. J., Illingworth, G. D., et al. 2022, *ApJ*, 935, 94
- Stefanon, M., Yan, H., Mobasher, B., et al. 2017, *ApJS*, 229, 32
- Sullivan, J. M., Hirano, S., & Bromm, V. 2018, *MNRAS*, 481, L69
- Tacchella, S., Bose, S., Conroy, C., Eisenstein, D. J., & Johnson, B. D. 2018, *ApJ*, 868, 92
- Tacchella, S., Finkelstein, S. L., Bagley, M., et al. 2022, *ApJ*, 927, 170
- Vijayan, A. P., Lovell, C. C., Wilkins, S. M., et al. 2021, *MNRAS*, 501, 3289
- Virtanen, P., Gommers, R., Oliphant, T. E., et al. 2020, *NatMe*, 17, 261
- Wilkins, S. M., Feng, Y., Di Matteo, T., et al. 2017, *MNRAS*, 469, 2517
- Wilkins, S. M., Stanway, E. R., & Bremer, M. N. 2014, *MNRAS*, 439, 1038
- Wilkins, S. M., Vijayan, A. P., Lovell, C. C., et al. 2022, arXiv:2204.09431
- Yan, H., Windhorst, R. A., & Cohen, S. H. 2003, *ApJL*, 585, L93
- Yung, L. Y. A., Somerville, R. S., Ferguson, H. C., et al. 2022, *MNRAS*, 515, 5416
- Yung, L. Y. A., Somerville, R. S., Finkelstein, S. L., et al. 2020, *MNRAS*, 496, 4574
- Yung, L. Y. A., Somerville, R. S., Finkelstein, S. L., Popping, G., & Davé, R. 2019, *MNRAS*, 483, 2983
- Zavala, J. A., Buat, V., Casey, C. M., et al. 2022, arXiv:2208.01816